# UNIVERSITÀ DEGLI STUDI DI PADOVA

Dipartimento di Fisica e Astronomia "Galileo Galilei"

Master Degree in Astrophysics and Cosmology

**Final Dissertation**

# Search for exoplanets through pulsation timing of Delta Scuti stars in the first PLATO field

**Thesis supervisor**
Prof. Giampaolo Piotto

**Thesis co-supervisor**
Dr. Valerio Nascimbeni

**Candidate**
Utsav Bose

**Academic Year 2023/24**

# Acknowledgments

Firstly, I would like to extend my heartfelt gratitude to my supervisor, Prof. Giampaolo Piotto, and my co-supervisor, Dr. Valerio Nascimbeni, for giving me the opportunity to work on this thesis. Your guidance and advice have been instrumental in helping me learn about my area of interest and apply my knowledge to this unique topic.

I thank my parents for their unwavering encouragement and trust in me throughout my academic career. They have motivated me to pursue my passion and have always supported me unconditionally.

I would also like to express my gratitude to my friends in Padova and my flatmates. Their companionship made my journey through the Master's program easier and more enjoyable.

# Table of Contents

**Abstract**

The PLATO mission to be launched in 2026 by ESA is a crucial mission for the advancement of exoplanetary studies. Prior studies of the field of view are important to identify the most important targets to be selected. The Pulsation Timing (PT) method, takes into account the light time travel effect (LTTE), on a pulsating star from an unseen companion. Out of many methods of exoplanetary detection, this method is so far a less exploited technique. The PT technique favors massive and far-away companions. Ideally, a long baseline of photometric data is needed. In this work, I apply the Pulsation timing method to analyze TESS 2min cadence light curves of Delta Scuti variable stars, which have a very short pulsation period(0.02 to 0.25 days). Starting from the list of all the known Delta Scuti stars in the first PLATO field, I selected bright targets ($T_{mag} < 13$) with more than 10 TESS sector data, and studied in depth two favorable stars (TIC349972148 and TIC308396022) as a pilot study. Using the VARTOOLS program, I first filtered TESS light curves of the candidates and computed their periodogram. Then I fitted a harmonic curve based on the fundamental pulsation period of the stars, and analyzed the $O-C$ plot to search for phase shifts of the main pulsation mode, as a function of time. Any detected periodic variation of the phase shift may indicate the presence of a secondary companion. For TIC308396022, I detected a secondary stellar companion of mass $0.41 \pm 0.03 M_{\odot}$, orbital period $803.4 \pm 0.2$ days and projected orbital semi-major axis $1.93 \pm 0.06$ AU. For both the candidates I did not detect any other perturbing companion, but I was able to explore the parameter space to confirm the absence of any secondary companion in the brown-dwarf mass range (and above) having a period greater than 100 days. The inaccuracy of the absolute TESS timestamps and the absence of a long baseline observation of the targets proposed limitations to the PT method. However, these will be improved by observations from the PLATO mission.

# Chapter 1

# Introduction

With the advent of new telescope technologies and space missions such as the Transiting Exoplanet Survey Satellite (TESS) mission (Ricker et al., 2015) and the recent James Webb Space Telescope (JWST) mission (Gardner et al., 2006), we are learning rapidly about extrasolar planetary systems. The study is going to get a boost in a couple of years with the launching of the Planetary Transits and Oscillation of stars (PLATO) mission (Rauer et al., 2014) by ESA. The possibility of finding planetary systems much similar to ours, being a host to life is an overwhelming opportunity that all humanity is curious about. The first step in the study of these extrasolar planets requires their detection. There are many detection methods developed over time by scientists, the most fruitful of them being the transit method and the radial velocity method. One of the most unexplored methods of detection of such planets is the Pulsation timing (PT) method, which takes into account the Light Time Travel Effect (LTTE) induced by the presence of unknown perturbers. In this thesis work, I have applied the PT method on the first PLATO observation field as an initial search, for targets that the mission will be observing with a long baseline. The phase shift of the pulsation signal of variable stars is observed and analyzed to detect possible perturbers.

This first chapter of this thesis contains an introduction to the main astrophysical objects involved in the analysis. Chapter 2 describes the space missions involved with the observations of such data. Chapter 3 includes the target selection and data analysis of the targets. Chapter 4 shows the Results and the Discussion while Conclusions are in Chapter 5.

## 1.1 Extrasolar Planets

Planets outside our Solar System are called extrasolar planets, or exoplanets. These planets either orbit around a star just like the planets in our Solar System, or

they might be unbound to stars and floating freely in space. The various detection methods of the extrasolar planets are:

- Imaging - Taking direct images by observing a planetary system. The planets are usually observed as point-like sources of light (either reflected from the host star or from its own thermal emission). This is usually done at infrared wavelengths and/or using a coronograph.

- Astrometry - This is done on planetary systems by measuring the transverse component of a host star. It involves observing the positional change in the photo centre of the star about its barycentre due to the presence of a perturber.

- Microlensing - When two stars align themselves closely, the star closest to the observer acts as a lens to warp the light coming from the background star. This creates a magnification of the latter and increases the apparent brightness of the two sources combined. So we see a peak forming due to the increase in flux. If there is an exoplanet or a floating planet, it will also warp the light around it and form minor peaks of magnification.

- Timing Variations- In this method exoplanets are detected by observing deviations in the expected timing of regular astronomical phenomena. This phenomenon could be the orbital period of already known transit planets (Transit time variations: TTV) or the periods of eclipsing binaries (Eclipse timing variations: ETV). In a specific case, the presence of planets around a variable star causes a change in the phase of its pulsating period. This is called the pulsation timing method. My thesis employs the Pulsation Timing variation method to detect planets which is explained in Section 1.3 in more detail.

- Radial Velocity - Stars move along their barycentre due to the Keplerian motion produced by a perturber. If the motion is along the line of sight of an observer, the stellar motion can be seen on a spectrograph as a Doppler shift in the spectral lines. From the Doppler shift, we can get the radial velocity and the period thus we can get planetary parameters like the minimum mass.

- Transit Method - When a planet comes in the line of sight between an observer and the host star, transit occurs. The transit reduces the amount of flux coming from the host star which can be measured as a dip in the light curve. This method favors planets near the stars and they have shorter time periods. From this method, we can get the radius of the planet, as well as some of its atmospheric properties as well.

The Transit method and the Radial method are the most common and successful methods in detecting exoplanets. They are complementary to each other as one

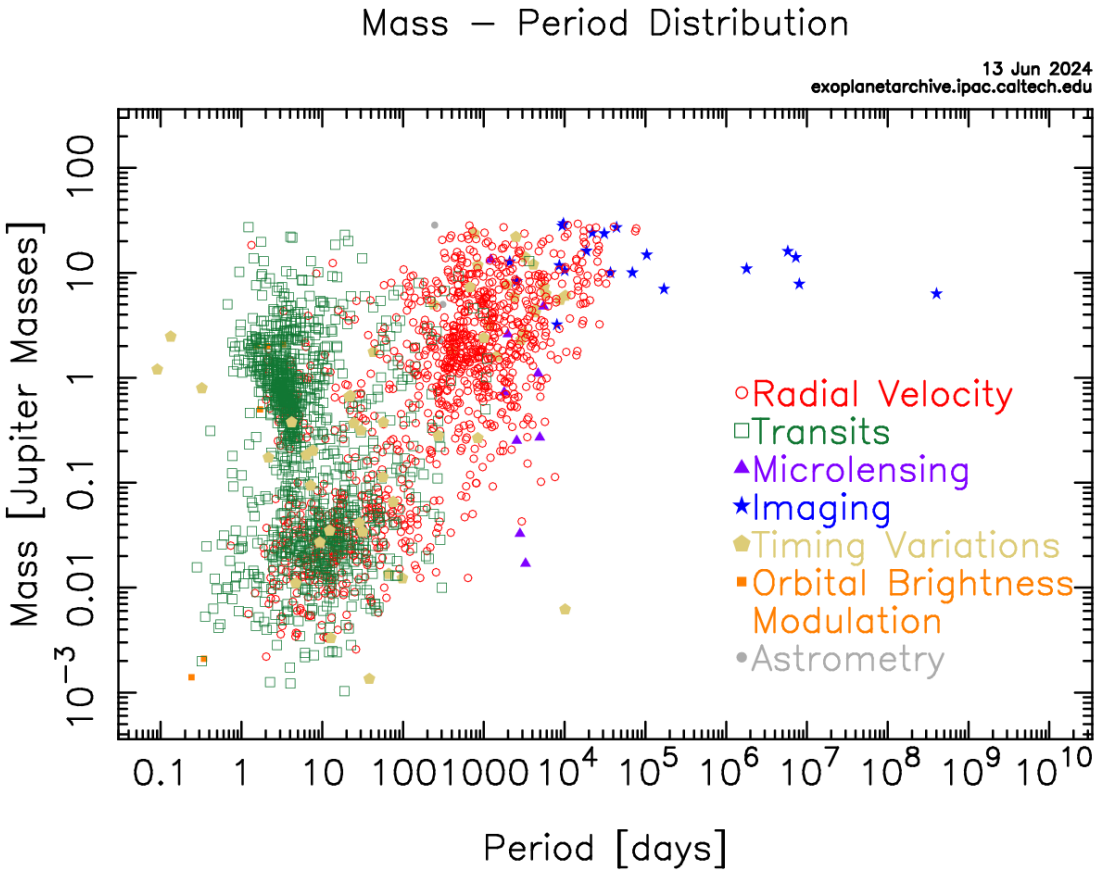


Figure 1.1: All discovered planets through various detection methods. Image credit: https://exoplanetarchive.ipac.caltech.edu/exoplanetplots/

gives the mass of the planet and the other gives the Radius. Using both we can get the density of planets and know about the inner structures of planets.

## 1.2 Pulsating Stars

Variable stars are stars which undergo periodic changes in their brightness when we observe them. They can be categorized into intrinsic variable stars and extrinsic variables. The extrinsic variables change their brightness due to phenomena external to the star, whereas the intrinsic variables (e.g. pulsating stars) vary their brightness due to phenomena occurring inside the star. These changes occur due to the expansion and contraction of the outer layer of stars.

### 1.2.1 Delta Scuti stars - pulsation mechanism

Delta Scuti stars are one of such Pulsating stars. The pulsations of Delta Scuti stars are driven by the heat engine driving mechanism caused by an increased opacity in their surface layers. This is called the Kappa mechanism where an increased level of opacity in the stellar atmosphere blocks the outward flow of radiation. The blocked flux causes a layer of gas to heat up, which increases the internal pressure such that the layer expands to return to equilibrium with its surroundings. Eventually, the gas within the layer will become ionized (mainly He II), reducing the opacity so that the layer is no longer opaque and the radiation flows through again. Having expanded beyond its equilibrium point and no longer being heated, the radial layer cannot support the weight of the overlying stellar atmosphere and contracts once again. The contraction allows the ionized gas to recombine and absorb the stellar flux, regenerating the source of opacity once again. Thus, a piston-like driving mechanism is created with heat being gained upon compression and energy being released upon expansion of a layer of gas in a star's atmosphere. This is the radial mode of pulsation. However, there are several other non-radial modes of pulsation that occurs in the Delta Scuti stars. Non-radial pulsation modes can be classified into pulsation quantum numbers ***n, l, m*** where they represent the number of radial nodes, the number of nodes in the stellar surface, and the number of nodes that are intersected while moving across the equator respectively. Gravity and pressure being the main driving and damping forces for stellar oscillation, the oscillations can also be classified into pressure modes ($\boldsymbol{p}$) and gravity modes ($\boldsymbol{g}$). Pressure modes are in the radial direction where as gravity modes are in the transverse direction (Handler, 2013). Pulsation modes of Delta Scuti stars may vary from a few radial nodes to hundreds of radial and non-radial nodes. This amplitude of the modes help study the stellar structures of the stars in great detail (Breger, 2000)(Bowman, 2017).

### 1.2.2 Properties of Delta Scuti stars

Delta Scuti stars are in the intersection of the classical Cepheid instability strip and the main sequence or they are moving towards the giant branch. They are mostly core hydrogen or in their hydrogen shell burning stage (C.Aerts, 2010). They have a spectral class between A and F with a mass range from $1.5M_{\odot}$ to $2.5M_{\odot}$. Their pulsation period ranges from 0.02 days to 0.25 days corresponding to radial and non-radial $p$ and mixed modes of low radial order. The RR Lyrae stars have similar periods and are distinguished from Delta Scuti stars because of the slow rotation of the Delta Scuti stars whereas RR Lyrae stars have no rotation.

Delta Scuti stars have 2 specific subgroups:

- HADS stars - They are High Amplitude Delta Scuti stars which are radial pulsators, having a peak-to-peak $V$ magnitude variation greater than 0.3 mag-

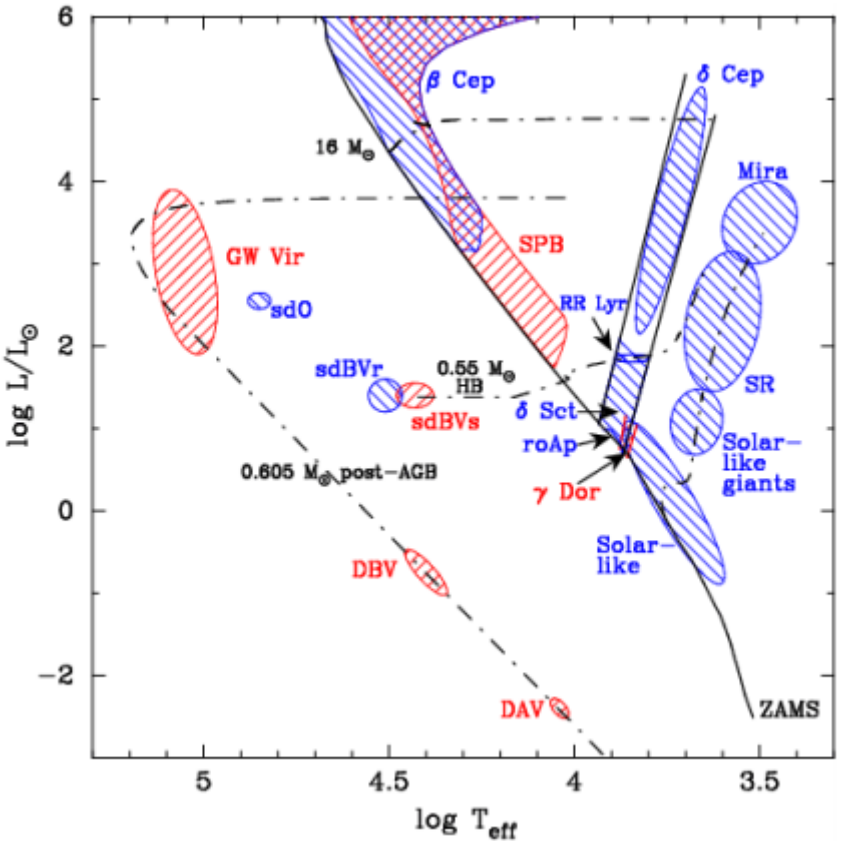


Figure 1.2: The Hertzsprung-Russell Diagram of pulsating stars. The Zero-Age Main Sequence is indicated as a full line, as is the classical instability strip (tilted from lower left to upper right). Some representative model evolutionary tracks are indicated as dash-dotted lines. Figure taken from Handler (2009).

nitudes. They have asymmetric light curves with a period of 1-6 hours. They are found in a narrow region of the classical instability strip. Detecting HADS stars is easier as they pulsate at a much higher amplitude than average Delta Scuti stars

- SX Phe stars - They are Population II variable stars within the classical instability strips. They have pulsation amplitudes and periods similar to Delta Scuti stars, but can be distinguished from them due to their low metallicity ([Fe/H]$< -0.5$)(McNamara, 1995) (Bowman, 2017).

## 1.3 Pulsation Timing Technique

The Pulsation Timing Method offers a complementary approach to detecting exoplanets by using the precise timing of pulsations in pulsating variable stars. Pulsating stars, such as RR Lyrae and Delta Scuti variables, exhibit a strictly periodic signal in their brightness. These pulsations serve as astrophysical clocks, allowing to detect subtle deviations caused by the presence of any orbiting companion.

At the heart of the Pulsation Timing Method lies the principle of timing variations induced by the gravitational influence of orbiting exoplanets. As a pulsating star undergoes its characteristic brightness fluctuations, the presence of an exoplanet can perturb its pulsation phase, causing a measurable phase change in the pulsation period. Considering a perturber on a circular orbit, the equation describing the Light time travel (LTT) delay is

$$A \simeq \frac{a \sin(i) m_p}{c M_*} \tag{1.1}$$

where $A$ is the semi-amplitude of the light time travel delay, $i$ is the inclination angle of the orbit, $a$ is the semi-major axis, $m_p$ is the mass of the companion, $M_*$ is the mass of the star and c is the speed of light. The time delay can be described as a Fourier series of sinusoidal functions such as

$$\tau = \sum_{k=1}^{N} A_k \sin\left(\frac{2\pi k T}{P_{orb}} + \phi_k\right), \tag{1.2}$$

where $A_k$ is the semi-amplitude of the signal, $P_{orb}$ is the orbital period and $\phi_k$ is the phase at a zero point. The harmonic nature of the LTTE signal, as inferred from this equation, can be investigated through a periodogram analysis of the LTTE signal from where we can identify the most prominent peaks.

After finding the most prominent pulsation frequency of the star from a periodogram of its light curve, the next step is to compute the phase shift from the light curve. This can be done using the $(O - C)$ method. Here the observed pulsation time $(O)$ is compared with the calculated value $(C)$ which was done using the average frequency signal. Ideally, the star has constant pulsation frequency so that any change in its phase is purely due to the presence of a companion. For such analysis when the perturber is a planet, frequency analysis should be done on all the frequencies of the stellar pulsation, as the companion will affect them equally. The equation for the residuals as given by (Hermes, 2018)

$$O - C = t_0 + \Delta P E + \frac{1}{2} P \dot{P} E^2 + A_1 \sin\left(\frac{2\pi E}{P_{orb,1}} + \phi_1\right) \tag{1.3}$$

where $t_0$ is the reference phase, $\Delta P$ is the overall uncertainty in the pulsation period, $\dot{P}$ is the pulsation period change, $\phi$ is the phase-variation phase, $A_1$ is the amplitude of phase variation occurring due to an external companion. E is the number of epochs calculated as $E = t/P$ where t is the observing time and $P$ is the pulsation period.

The key elements required for the search of exoplanets using the Pulsation Timing technique are:

1. The sensitivity of the PT technique totally depends on the choice of the variable star. The target should have high amplitude and short-period pulsations. A good phase stability makes the detection more precise. Delta Scuti stars are the most suitable for such observations (Compton et al., 2016) along with pulsating hot subdwarfs, and pulsating white dwarfs (Hermes, 2018).

2. The observation should have a long baseline covering at least one orbit of the host star around its barycentre. Longer observational time makes the PT technique more sensitive to detect smaller mass planetary companions.

The Kepler/K2 mission (Borucki et al., 2010) and the TESS mission have provided with near-continuous photometric time series data, which can be used to analyze for phase shifts.

### Discoveries using Pulsation Timing Method

Since more massive objects result in a larger change in the phase shift, the most common detection using the Pulsation Timing variations are unseen stellar companions. Hundreds of stellar companions have been detected around Delta Scuti stars and have been verified with Radial velocity follow-up (Compton et al., 2016)(Murphy et al., 2013). Until now Pulsation timing method has been able to discover only 2 confirmed planets, namely V0391 Peg b (Silvotti et al., 2007) and KIC 7917485 b (Murphy et al., 2016). The first planetary discovery was done in 2007 around V391 Pegasi by Silvotti et al. (2007). This is a hot subdwarf B star having short-period p-mode pulsations. From the observations, the sinusoidal variations of the residuals from the $O-C$ plot had no other explanation other than occurring due to the wobble of the star. The amplitude of the wobble is within the planetary regime, thus indicating the presence of a planet. The companion is found to have a minimum mass of $3.2 \pm 0.7 M_J$ and a period of about $1170 \pm 44$ days. Another discovery which is also the most recent one is KIC 7917485b discovered by Murphy, Bedding, and Shibashi in 2016. They analyzed the photometric light curve from the Kepler Mission of the main sequence A star located in the Delta Scuti instability strip. The observation data was a long 4 years. Applying the Pulsation Timing technique they

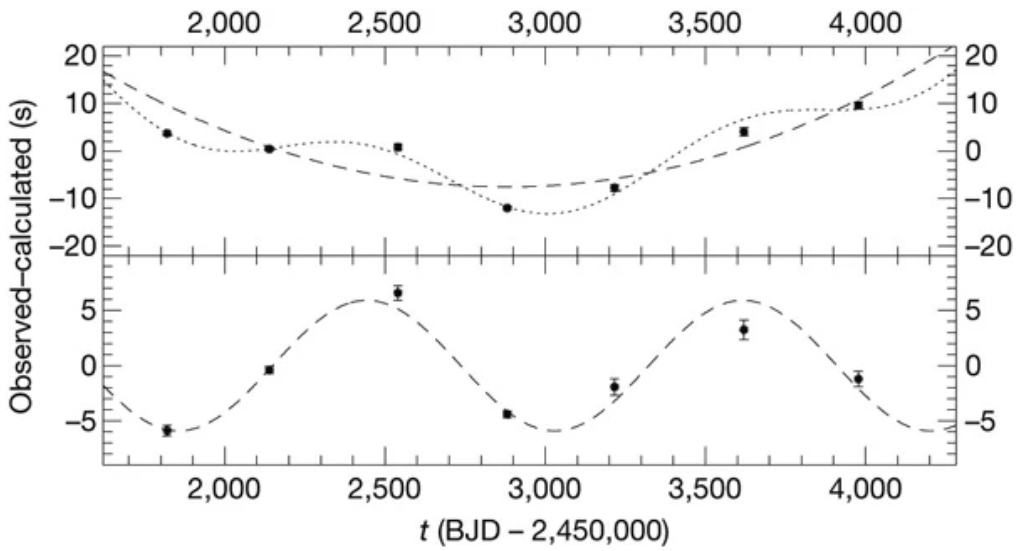


Figure 1.3: $(O-C)$ plot of V391 Pegasi taken from Silvotti et al. (2007). The upper and lower panels represent the $(O-C)$ diagram based on its fundamental frequency and its sinusoidal component respectively.

discovered a $M_{min} = 11.8 M_J$ planet, with a period of $840 \pm 20 days$ in the habitable zone.

Vaulato et al. (2022) have applied the Pulsation Timing method to suitable Delta Scuti stars and have detected candidate companions for two targets in the sub-stellar mass regime. They found a companion around Chang 134 having mass and period $43 \pm 5 M_{jup}, P \simeq 82d$, and around V393 Car ($> 100 M_{jup}, P > 700d$).

# Chapter 2

# Space Missions

In this chapter, I will review two important space missions related to my thesis work. These are the ongoing Transiting Exoplanet Survey Satellite (TESS) mission (Ricker et al., 2015), whose light curve data I have used for analysis in my thesis, and the upcoming Planetary Transits and Oscillation of stars (PLATO) mission (Rauer et al., 2014), which will benefit from the pre-mission analysis of the targets in its first field of view.

## 2.1 TESS

The TESS mission, launched by NASA on April 18, 2018, is dedicated to the discovery of exoplanets. It started its operation on 25th July 2018, and is performing a nearly all-sky survey to search for exoplanets. TESS is set on a high elliptical orbit with perigee and apogee of nearly $17R_{\oplus}$ and $59R_{\oplus}$ respectively. It orbits around the Earth nearly every 13.7 days, which is in a 2:1 resonance with the Moon. This was done to ensure that lunar perturbations do not affect it. The high orbit also ensures that TESS is far from the Earth's radiation environment, and not affected by Earth-Moon stray light.

The primary goal of TESS is to detect Super-Earths and Neptune-like exoplanets around nearby main-sequence, bright dwarf stars, of spectral types F5 to M5. This is an improvement over the previous Kepler mission by NASA, which observed stars that were too faint for follow-up observations.

The list of suitable targets to be observed is selected from the TESS Input Catalog(TIC) (Stassun et al., 2019). The TIC version 8 used the Gaia DR2 catalog as a base and merges other photometric catalogs such as 2MASS, SDSS, WISE, etc. It contains about 1.5 billion stars and their parameters. There has been an update to the TIC to version 8.2 recently (Paegert et al., 2021) which is the current version. The Candidate Target List (CTL) is a subset of the TIC where TESS is more likely

to detect a transit-like signal. This list is selected based on various components which I have discussed in Section 3.1.1.

### 2.1.1 Optical Design

The TESS telescope consists of four similar refractive cameras. Each of these cameras consists of a lens assembly, a detector assembly with four silicon charged-coupled devices (CCDs), and a lens hood to reduce scattered light from Earth and Moon. These four cameras are mounted onto a single plate. The lens assembly has four identical $f/1.4$ lenses having an entrance pupil diameter of 10.5cm. Each of these cameras covers a $24^o \times 24^o$ field of view of the sky (Figure: 2.2) making the TESS cameras together cover $24^o \times 96^o$ FOV.

In the detector assembly, each of the CCD array contains four back-illuminated MIT/Lincoln Laboratory CCID-80 devices. Each CCID-80 device consists of a 2048 x 2048 pixels imaging array, thus overall creating a 4096 x 4096 pixel imaging array together. Each pixel size is $15\mu m \times 15\mu m$ which corresponds to 21 x 21 arc-seconds in the sky. The operational temperature of the CCDs is $-75^oC$, where the dark current is negligible. Increased sensitivity to red wavelengths is needed for photometry around small, cool, and red stars, which made the CCDs have a band-pass of 600 nm to 1000 nm.

During observation, the TESS cameras produce continuous images of 2-second exposures, which the Data Handling Unit(DHU) processes in real time to convert raw CCD images to data products. These are then downloaded at a maximum of 6-hour gap during the orbit perigee.

### 2.1.2 Observation Strategy

The north and south ecliptic hemispheres have been divided by the TESS camera FOV into 13 partially overlapping sectors. Each of these sectors($\sim$ 28 days) is observed for two TESS orbits. During the primary mission (25th July 2018 to 4th July 2020), TESS completed observing both the hemispheres in 2 years (26 sectors). The sectors and the observation times are illustrated in Figure 2.2. Only a small 12 degree strip across the Ecliptic was left out. The ecliptic poles were observed by TESS for 350 days which is also the region JWST is observing continuously. The data products that were produced during these observations were 30-minute cadence full frame images and 2-minute cadence light curves.

From July 2020 to September 2022, TESS completed its first extended mission. During TESS cycle 3, it re-observed the southern ecliptic hemisphere from sectors 27-39. For TESS cycle 4, it observed the northern hemisphere for 15 months (sectors 40-55). Data products during cycles 3 and 4 that were produced are 2-minute

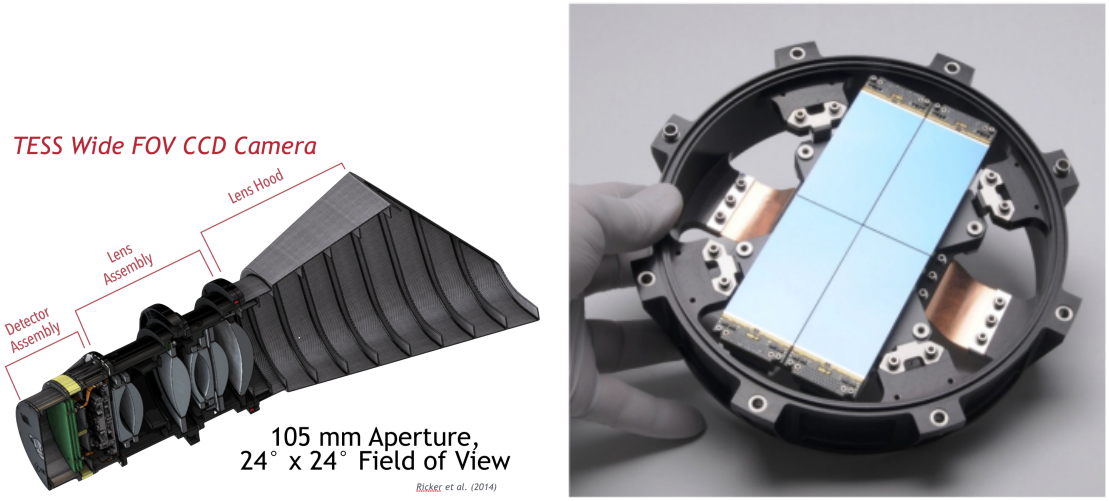


Figure 2.1: One TESS wide FOV CCD Camera (left), TESS CCD mosaic in mounting bracket (right). Image credit: https://heasarc.gsfc.nasa.gov/docs/tess/the-tess-space-telescope.html

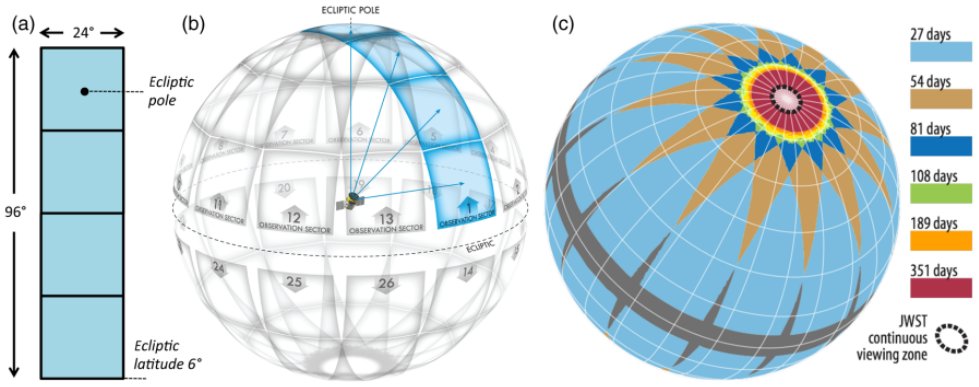


Figure 2.2: a) The combined field of view of four TESS cameras, b)Division of the celestial sphere into the observing sectors of TESS, and c)Duration of observations of the celestial spheres taking into consideration the overlaps of each sector. The dotted circle is the area that is continuously being observed by JWST. Image credit: Ricker et al. (2015)

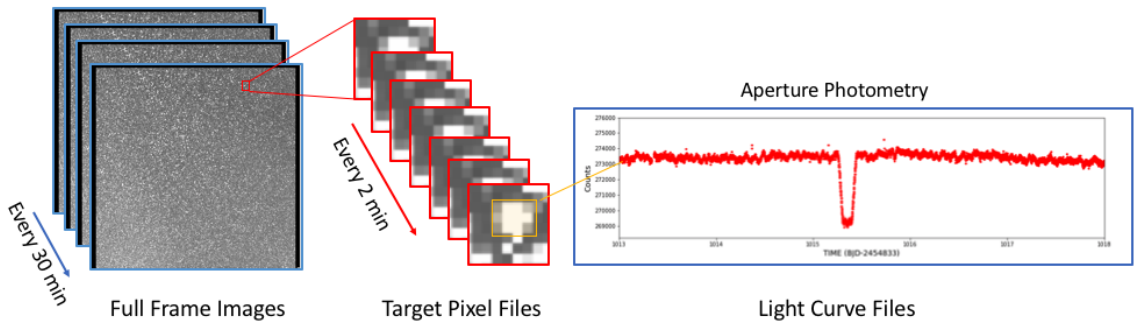


Figure 2.3: TESS photometric data products. Image credit: https://heasarc.gsfc.nasa.gov/docs/tess/data-products.html

cadence data for selected targets, 20-second cadence data for a selected number of targets, and 10-minute cadence full frame images.

The second extended mission, starting from September 2021 is planned to last 3 years. TESS is observing fields in both the northern and southern hemispheres. For cycle 5, it observed through sectors 56 to 69. The data products from this cycle included 2-minute cadence data, 20-second cadence data, and 200-second full-frame images. This is the latest data release that I have used in my thesis. Currently, TESS is in its cycle 6 phase.

### 2.1.3 Light Curve Data Products

The data products I used are the light curves of specific targets downloaded from the MAST website [1]. For these targets, TESS produces Target Pixel Files (TPF), which are raw data containing a grid of pixels around the target defined by an aperture mask. This is recorded every 2 minutes with a 2-second exposure for each image. These pixels are used to create the required photometric time series (light curve) of the target.

## 2.2 PLATO

The Planetary Transits and Oscillation of stars (PLATO) mission (Rauer et al., 2014) (Rauer et al., 2024) is a third medium-class mission in the ESA Cosmic Vision Programme (2015-2025). It is set to be launched at the end of 2026. The goal of this mission is to detect and characterize a large number of exoplanetary systems, which includes terrestrial exoplanets orbiting bright, solar-type stars in their habitable zones. With its high-precision photometry, it will be able to accurately

[1] https://archive.stsci.edu/kepler/data_search/search.php

determine planetary properties through transit method. The light curve will also aid in the precise determination of stellar properties and study of internal stellar structures with the help of asteroseismic analysis. PLATO will identify good targets for ground-based spectroscopic follow-up observations for a complete determination of the planetary properties such as mass and mean density. The results can be used to study the architecture of planetary system, and how the planets and planetary systems evolve over time.

### 2.2.1 Optical Design

PLATO will be observing bright stars, on which radial velocity measurements can be done through ground-based observatories. These stars are sparse in the sky, for which PLATO has a wide field of view of 2132 $deg^2$. The photon collection area is split into 26 cameras, out of which 24 ("normal cameras") are used for science operations and 2 ("fast cameras") are used for fine-pointing and science operations. The 24 normal cameras are aligned in groups of 4, with 6 cameras in each group. The cameras are identical, 20 cm class telescopes with an entrance pupil of 12 cm and optimized for a single 500-1000 nm bandpass. Each of the normal cameras has a total field of view of 1037 $deg^2$. The line of sight of each of the 4 groups is offset by $9.2^o$ with respect to a central line of sight. This creates a pattern as shown in Figure 2.4, which shows that different regions in the field of view are monitored by 24, 18, 12, and 6 cameras at a time. Due to the overlapping of cameras, the central region being observed by more cameras will provide greater photometric precision than the peripheral ones. The 2 fast cameras will be centered on the central line of sight, which will observe the inner region and provide color information with a faster sampling cadence of 2.5sec, whereas as the normal cameras will work at 25 sec cadence. Each identical normal camera has 6 lenses and 4 full-frame CCDs of $81.8 \times 81.8 mm^2$ each on the focal plane. The total number of effective pixels per camera is $4150 \times 4150$ having size $18 \times 18 \mu m$, thus each pixel covering 15 arcsec.

### 2.2.2 Observation Strategy

PLATO will be launched into orbit around the L2 Lagrangian point. The primary science operation phase of PLATO is planned for four years, with an extension for up to 8.5 years. The four years of observation have been planned to be split into two observation phases of two years, called the Long Observation Phases (LOPs). Alternate possibilities are a longer field of three years or staring at one field for the entire science operation phase. The first field that will be observed by PLATO is the LOPS2 field (Nascimbeni et al., 2022) centered on the galactic co-ordinates l= 255.9375 deg and b = -24.62432 deg. This is the field whose targets I have analysed in this thesis.

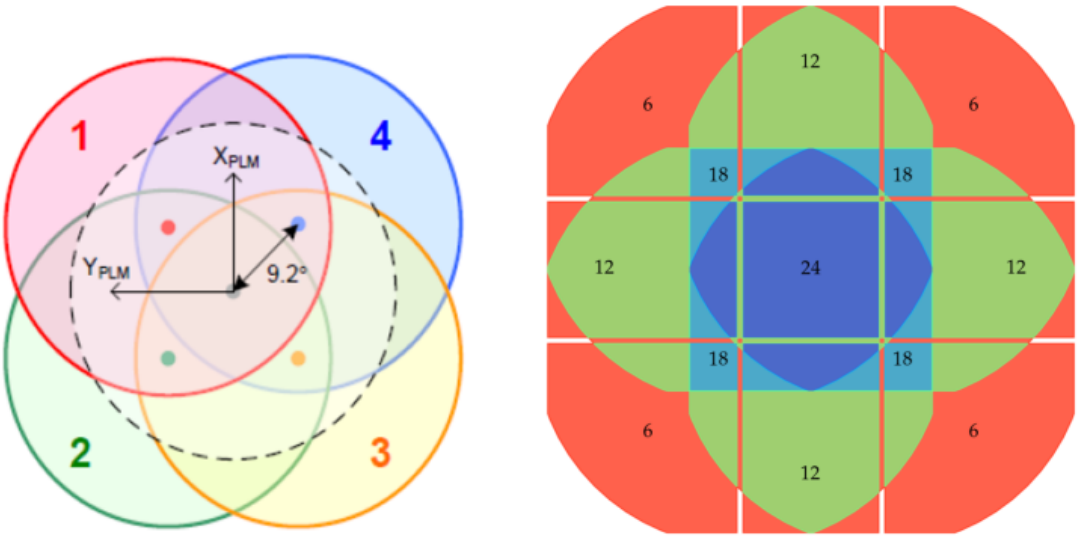


Figure 2.4: Illustration of the PLATO field coverage. Left: position on the sky of the optical axis of the four groups of 6 co-aligned "normal" cameras, and of the two "fast" cameras (dashed black line). Right: Number of "normal" cameras observing simultaneously the different sectors of the overall PLATO field of view. The center of the field (dark blue) is observed by all 24 cameras. At the edges (orange) only 6 cameras observe simultaneously the same field in the sky. Image Credit: Rauer et al. (2024)

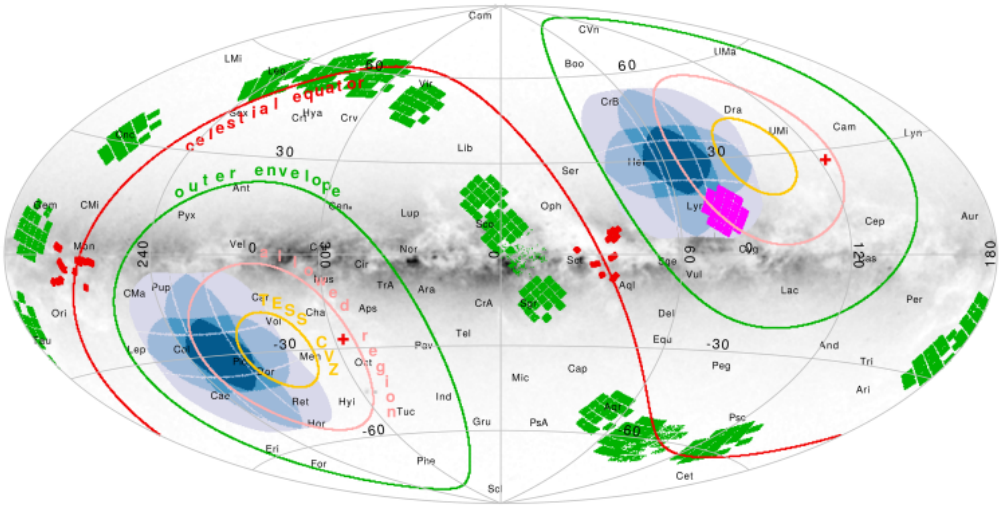


Figure 2.5: Illustration of PLATO FoVs (blue) in comparison to Kepler (pink), K2 fields (green) and CoRoT mission fields (red). Lines indicate the TESS viewing zones. The position of the PLATO fields is indicative only (figure reproduced from Nascimbeni et al. (2022))

The targets to be observed, which will constitute the PLATO Input Catalog (PIC) (Montalto et al., 2021) are decided two years before the launch with an update nine months before the launch. PLATO will download light curves of pre-selected targets, thus pre-mission in-depth analysis of targets in the field of view is very important to prioritize the targets. The targets are defined into four stellar samples:

- P1: main sequence and sub-giants stars in spectral type F5-K7, brighter than V=11, the noise level must be less than 50 ppm in 1 hr.
- P2: similar to P1 but brighter than V=8.5.
- P4: stars brighter than V=16 with spectral type M.
- P5: stars brighter than V=13, spectral type F5 to K7 with no constraint on photometric noise.

Thus, the PLATO mission with high-precision photometry and a long baseline time series data of bright stars, will provide crucial data which can be analysed for exo-planet search with the Pulsation Timing Technique.

# Chapter 3

# Analysis

The first long-duration field (LOPS2) of PLATO is already decided, and the uninterrupted light curve data from PLATO will have a huge potential for the Pulsation Timing technique. This is why I focused on Delta Scuti stars in the first PLATO field. In this thesis, I have analyzed TESS light curves of Delta Scuti stars within the LOPS2 as a preparatory pilot study. This is important because, unlike TESS, PLATO will not download full-frame images, but rather the targets have to be pre-selected in advance.

## 3.1 Target Selection

### 3.1.1 TESS CTL

A subset of the TESS Input Catalog(TIC) is the TESS Candidate List (CTL) where the data is downloaded on a short two-minute cadence along with cut-out images called Target Pixel Files (TPFs). It is a list of stars which are identified to be good candidates to host a transiting exoplanet. The main properties of such stars in the list (Stassun et al., 2019) are:

- All TIC stars brighter than T = 13 and have stellar radii estimated to be smaller than $5R_{\odot}$
- Should have reliable Gaia parameters
- Do not have TESS magnitudes or $T_{eff}$ suggesting the star to be a white dwarf.
- All stars that are listed in the curated cool Dwarf (CDC) (Muirhead et al., 2018) catalog.

The CTL list that I used as of December 2023 is CTL version 8 containing TESS light curves from sectors 1 to sector 69.

### 3.1.2 The Chang 2013 Catalog

The Chang 2013 catalog (Chang et al., 2013) has listed 1578 Delta Scuti stars in the Milky Way including both field stars and cluster members. The Catalog contains 718 stars (46%) from Rodríguez's work (Rodríguez and López-González, 2000) and the rest (54%) stars combined from other published works. The majority of the catalog stars are characterized as having a pulsation period between 0.02 to 0.25 days (Figure 3.1), pulsation amplitudes ($< 0.5$ mag), and spectral types A–F.

A list of surveys from which the stars in Chang 2013 are taken are listed in Table 3.1.

The important catalog parameters that are relevant for this thesis work are

- Right Ascension (RA) and Declination (DEC) are the coordinates of the targets given in reference to the J2000 epoch. The Right Ascensions are in the format of hours:minutes:seconds, and Declination is in the format of degree:minutes:seconds.
- Period is in units of days. The period provided in the catalog is the fundamental period of the stars. In the case of multiple periods, the dominant period is given.
- Magnitude is given for the $V$ and $B$ band filters. This provides an idea about how much bright the star is. The brighter it is, the lower the photon noise and the more accurate will be the observation, with every other source of error being equal. Also, the $\delta V$ mag is given.
- The Spectral Type of the star is provided for most of the stars, which is a proxy for the effective temperature of the stars too.
- Binarity: The catalog provides a flag that is "1" if it is a binary system and "0" if it is a single system.

### 3.1.3 Matching Catalogs

I matched the TESS CTL with the Chang 2013 catalog to get a list of all the Delta Scuti stars that have been observed by TESS. I did this using TOPCAT setting a matching positional error margin of 10 arcseconds. We need an increased margin to cross-match because the proper motion epochs in the TIC are not always the same, as they come from a merge of different catalogs. Also, each TESS pixel is about 21 arcseconds thus stars within 10 arcseconds will still be in the same pixel. After matching, I also verified from the light curves that all the stars are Delta Scuti stars. Additional data available for each star from the TESS CTL are

| Sources | Number of stars[b] | References |
|---|---|---|
| Hippacros | 78 | Perryman et al. (1997) |
| OGLE[c] | 52 | Udalski et al. (1997) |
| MACHO[d] | 81 | Alcock et al. (2000) |
| ROTSE[e] | 4 | Jin et al. (2004) |
| ASAS[f] | 525 | Pojmanski et al. (2006) |
| TAOS[g] | 41 | Kim et al. (2010) |
| GCVS[h] | 419 | Samus et al. (2009) |
| Open clusters | 92 | List A[i] |
| Globular clusters | 204 | List B[j] |
| Miscellaneous | 82 | Individual papers |
| Total | 1578 | - |

Table 3.1: List of surveys from which the Chang 2013 catalog was made. Table is taken from Chang et al. (2013) , Table 1.

*Notes. The catalog is build up on stars compiled by R2000 and Rodríguez and López-González (2000).*

[b] *This number (Column 2) is inclusive of both pre-existing Rodríguez and López-González (2000) and newly listed Delta Sct stars.*

[c] *Optical Gravitational Lensing Experiment.*

[d] *MAssive Compact Halo Object.*

[e] *Robotic Optical Transient Search Experiment.*

[f] *All-Sky Automated Survey.*

[g] *Taiwan-American Occultation Survey.*

[h] *General Catalog of Variable Stars.*

[i] *List A: alpha Persei, Pleiades, Hyades, Praesepe, Melott 71, NGC 2682, NGC 3496, NGC 5999, NGC 6134, NGC 6882, NGC 7062, NGC 7245, NGC 7654, IC 4756.*

[j] *List B: omega Cen, 47 Tuc, IC4499, M3, M4, M5, M13, M15, M53, M55, M56, M68, M71, M92, NGC 288, NGC 3201, NGC 4372, NGC 5053, NGC 5466, NGC 5897, NGC 6362, NGC 6366, NGC 6397, NGC 6752, Ru 106.*

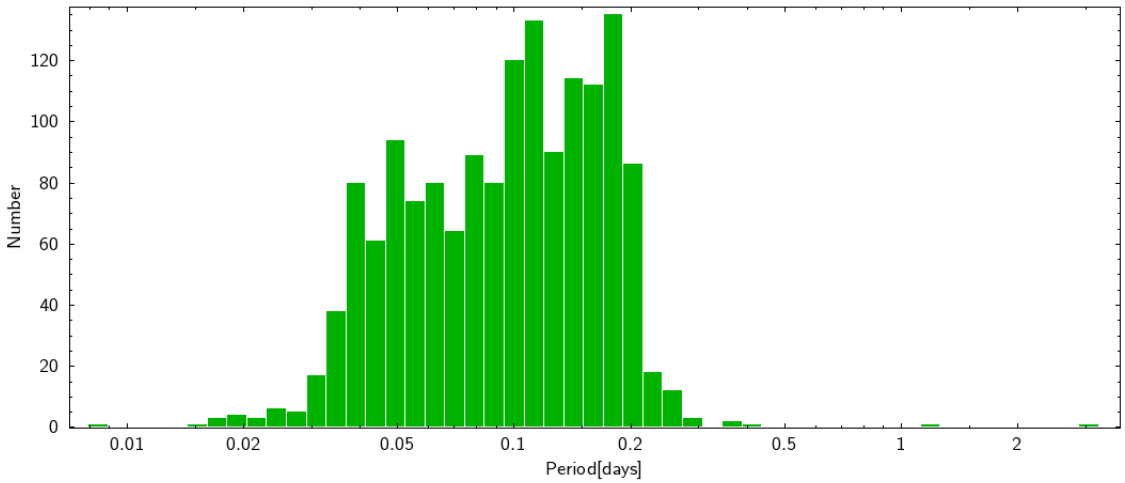


Figure 3.1: Distribution of periods of all stars in the Chang 2013 Catalog.

- TIC: TESS Input Catalog ID which identifies the target in the TESS catalog with a unique ID.
- TESS magnitude;
- N: Number of TESS sectors the target was observed for.

Because my aim is to study the stars in the first PLATO field, for which I applied the LOPS2 galactic coordinates to select only the first field of view stars in PLATO. For this, in TOPCAT I used the expression "inSkyEllipse(l,b,255.9375,-24.62432,28.1,28.1,0) and inSkyPolygon(l,b,288.6075,-44.1,223.2675,-44.1,233.1675,-0.25,278.7075,-0.25)", which restricts the FOV along an eclipse and a quadrilateral which approximately denotes the first PLATO field. (Figure 3.2) We also need stars with a long observation baseline for the PT technique to be more sensitive, so another condition was applied which is selecting stars observed by TESS for more than 9 sectors. I got a total of 9 stars (Table 3.2) after putting these conditions and cross-matching the table.

### 3.1.4 Final Sample of stars

I downloaded one sector light curve for each target in our sample and plotted them to check if they actually fit the Delta Scuti class for short-period pulsations. Out of all the stars, I found stars TIC 260654645, TIC 364399376, and TIC 38515566 were already analyzed for PT Method by Vaulato et al. (2022) who used the same technique and software tools that I am using in my thesis. I also did an initial analysis on these targets which resulted in the same fundamental period that Vaulato

| TESS ID | RA [hours] | DEC [deg] | Mass $[M_\odot]^a$ | Spectral Type | $T_{mag}$ | N | Period [d] |
|---|---|---|---|---|---|---|---|
| 349972148 | 114.67 | -61.8188 | 2.15 ± 0.10 | - | 10.16 | 10 | 0.1685 |
| 38515566 | 62.7659 | -63.1605 | 1.75 ± 0.13 | Fm / delta Del | 8.85 | 13 | 0.1228 |
| 41232835 | 91.9808 | -66.3597 | 0.98 ± 0.01 | k1IV(e) | 10.17 | 14 | 0.1197 |
| 364399376 | 119.761 | -61.5834 | 2.02 ± 0.10 | A7III/IV | 7.16 | 19 | 0.1413 |
| 308396022 | 120.2598 | -63.675 | 1.50 ± 0.13 | - | 11.07 | 22 | 0.0757 |
| 260654645 | 98.1884 | -57.8055 | 1.68 ± 0.14 | - | 12.44 | 23 | 0.091 |
| 25195864 | 63.7536 | -69.5367 | 1.98 ± 0.18 | A2III/IV | 10.39 | 24 | 0.2 |
| 279361762 | 104.7667 | -58.5147 | 2.07 ± 0.03 | Fm / delta Del | 8.04 | 24 | 0.12 |
| 38587180 | 64.1641 | -64.3154 | 1.81 ± 0.15 | F0III | 7.69 | 25 | 0.067 |

Table 3.2: List of all the 9 targets shortlisted after matching the TESS CTL and Chang 2013 catalogs and putting the condition for presence in the first PLATO field.
Note $^a$: Data taken from StarHorse2 Catalog. (Anders et al., 2022)

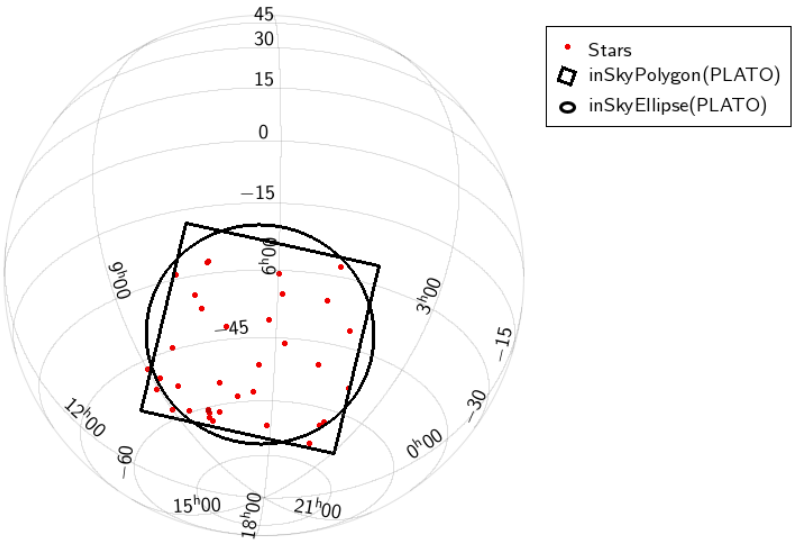


Figure 3.2: 39 Delta Scuti stars available (red points) after matching the Chang 2013 catalog and the TESS CTL, included in the first PLATO field (LOPS2; its approximate footprint is within both the spherical square and circle plotted with a thick black line).

et al. (2022) had extracted. So I discarded them from further analysis. All the targets that I have selected have $V$ magnitude $\leq 11$, which provides a bright observed flux for each target. This was done to avoid being limited too much by photons and background noise. All the stars in the final list have Delta Scuti-like light curves.

## 3.2 General Analysis of all targets

### 3.2.1 Extraction and Pre-conditioning of Light Curve

The light curves of the targets are downloaded from the MAST[1] archive.

The light curves are extracted from each observing sector of TESS's 2-minute short-cadence observation. A faster cadence data like the fast 20 sec cadence data, which was collected during the extended mission, can also be useful for this analysis. For this thesis purpose the 2-minute cadence data can very well sample the Pulsation of Delta Scuti stars thus I have used that. Two kinds of photometric data are provided from TESS, one is the Simple Aperture Photometry (SAP) Flux and the Pre-search data conditioning Simple Aperture Photometry (PDCSAP) Flux. The SAP light curve is calculated by summing all the calibrated flux of the pixels that

[1] https://archive.stsci.edu/kepler/data_search/search.php

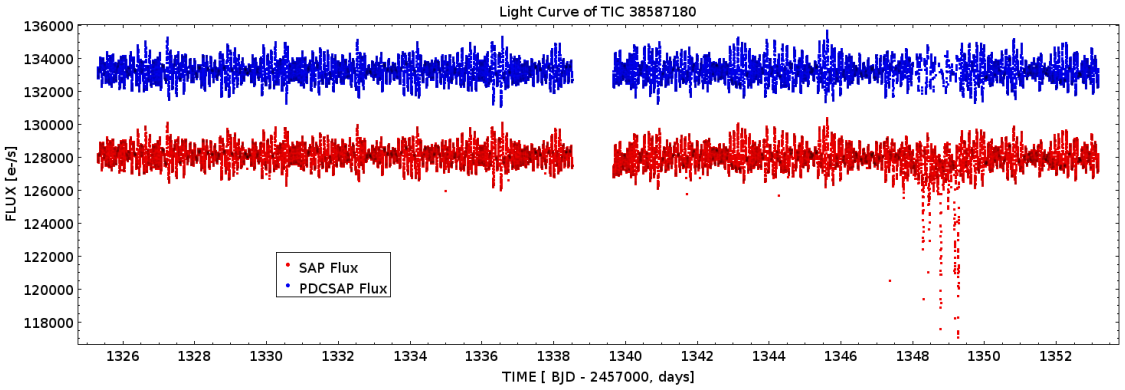


Figure 3.3: Plot showing the difference between the SAP flux and the PDCSAP flux of TIC38587180.

fall within an aperture set by the TESS mission. PDCSAP is a post-processed data from SAP, which is much improved, by removing long-term trends and having fewer systematic errors. Ii is usually a better choice for detecting planets. I used the PDCSAP flux for further analysis which I checked with the SAP flux to verify that there are not many changes other than correction for systematic errors. As VARTOOLS works in magnitude space, I converted the PDCSAP flux to magnitudes. I discarded all the points that were flagged q≠0, which gives all the points that were taken during an anomalous event. I have applied an iterative $15\sigma$ clipping to the light curve to discard the most extreme outliers. The sigma clipping is performed over the mean.

The TESS, after each 13.7 days is at the perigee of its elliptical orbit. Here it orients itself for a data download of about 3 hours and then re-orients itself to continue its mission. I have separated the TESS observations of the light curves of each sector into "orbits" of 14 days, corresponding to one orbit of TESS around the Earth. This is done as the choice of the segment size is a trade-off between time resolution and frequency resolution. Murphy et al. (2013) found that 10-day segments gave enough frequency resolution to measure phases of well-resolved pulsation modes, while still giving enough time resolution to monitor the time-delays.

### 3.2.2 GLS Periodogram

The Lomb-Scargle Periodogram is a well-known tool for frequency analysis in a unequally sampled time series data. It is equivalent to fitting a sine wave function of the form $y = a\cos\omega t + b\sin\omega t$. For this thesis, I have extracted the Generalized Lomb Scargle Periodogram (Zechmeister, M. and Kürster, M., 2009). Compared

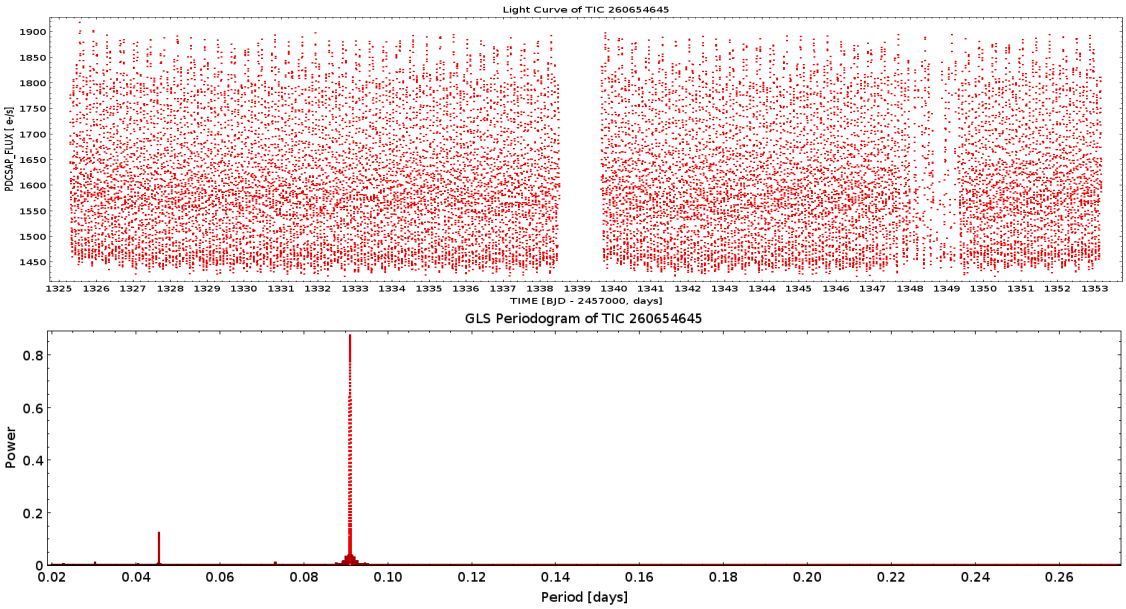


Figure 3.4: One sector (two orbits) light curve(above) and GLS Periodogram (below) of TIC260654645 (TESS Sector 1).

to the LS periodogram the GLS periodogram provides more accurate frequencies, is less susceptible to aliasing, and gives a better determination of the spectral intensity. It allows for a floating mean and also non-uniform errors. GLS periodogram takes into account several frequency analysis methods that already exist such as Discrete Fourier Transform, floating mean periodogram, and "spectral significance" estimator using the SigSpec program.

I have analyzed the light curves of the first sector of each target and did an initial GLS periodogram in the range of 0.01 to 28 days, to find the fundamental pulsation mode of the star. The choice of this range is because Delta Scuti stars will not have periods below 0.01 and the TESS sectors are each of 28 days, thus it will not be possible to detect periods above 28 days. The periodogram also finds if there are other strong pulsation modes which might interfere with the analysis, and it also gives details about the stellar vibration modes.

From the initial periodograms of the targets, I realize that TIC279361762 (Figure 3.8) and TIC38587180 (Figure 3.7) have a very complex spectrum. It does not have one single fundamental pulsation mode but has many pulsation mode with varying amount of strength. For TIC279361762 (Figure 3.8), even though it has one of the pulsation modes at a relatively greater strength than the others it is not enough to be distinguished as the fundamental Pulsation mode. I also found that there is a discrepancy in the fundamental period that I found from my analysis

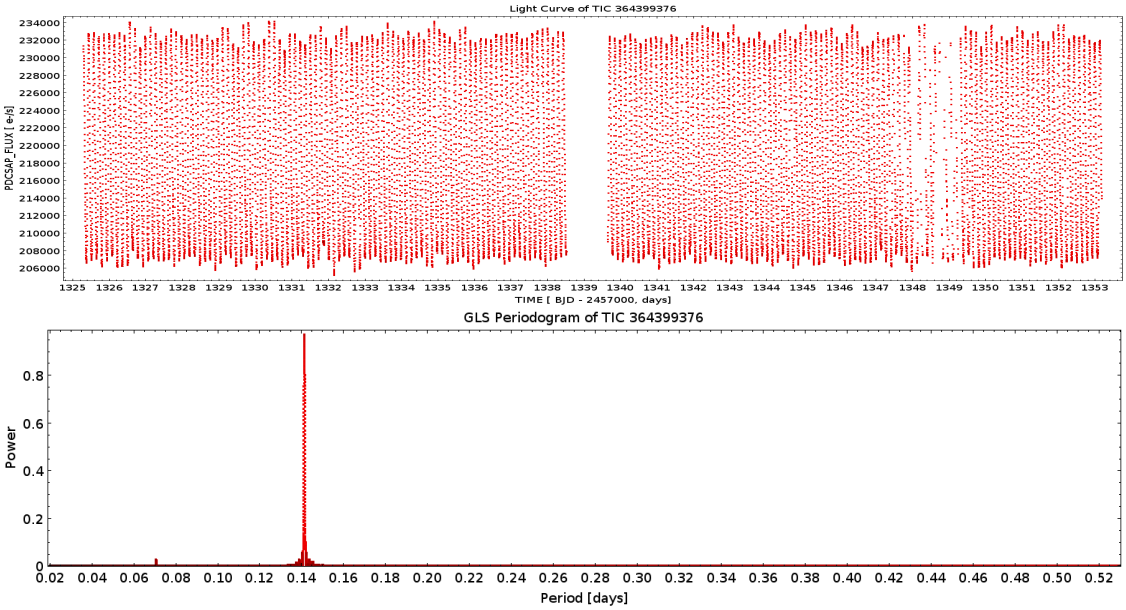


Figure 3.5: One sector (two orbits) light curve(above) and GLS Periodogram(below) of TIC364399376(TESS Sector 1).

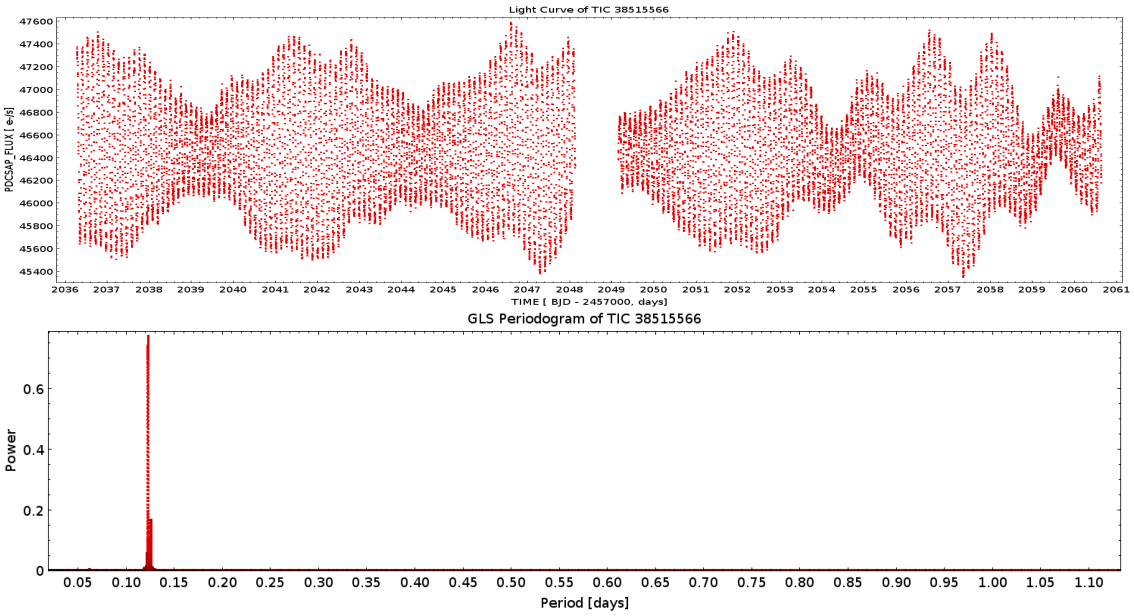


Figure 3.6: One sector (two orbits) light curve(above) and GLS Periodogram(below) of TIC38515566 (TESS Sector 27) .

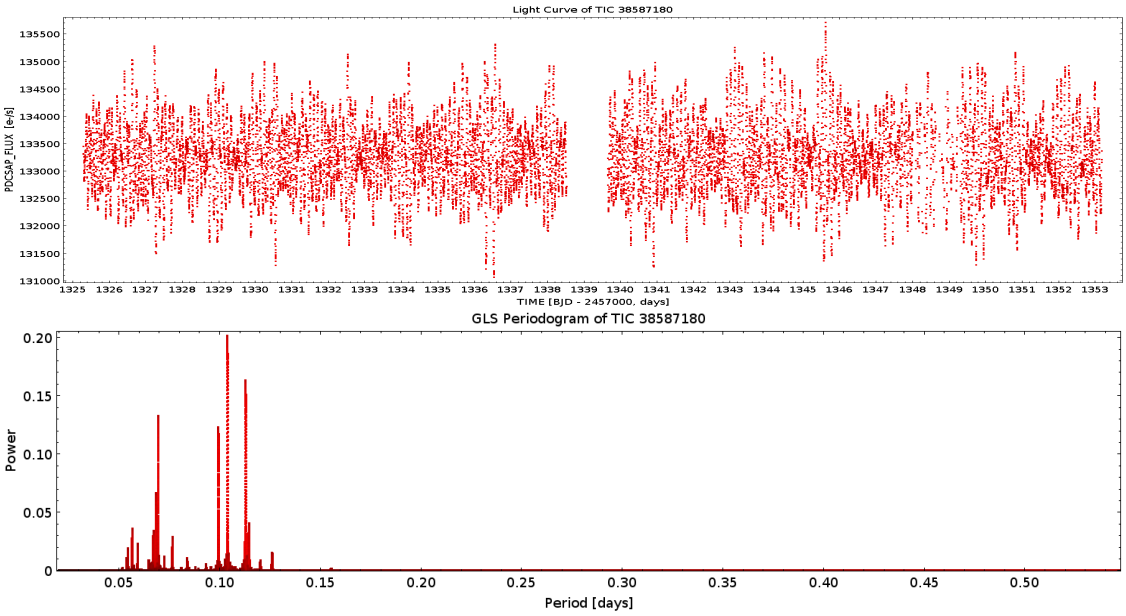


Figure 3.7: One sector (two orbits) light curve(above) and GLS Periodogram(below) of TIC38587180 (TESS Sector 1).

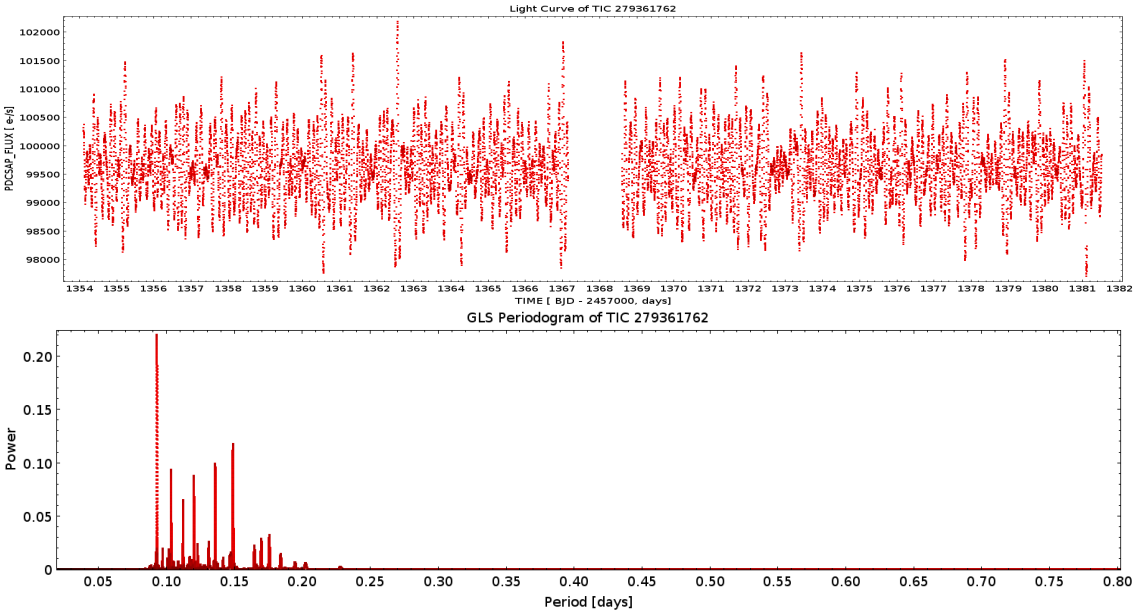


Figure 3.8: One sector (two orbits) light curve(above) and GLS Periodogram(below) of TIC279361762 (TESS Sector 2).

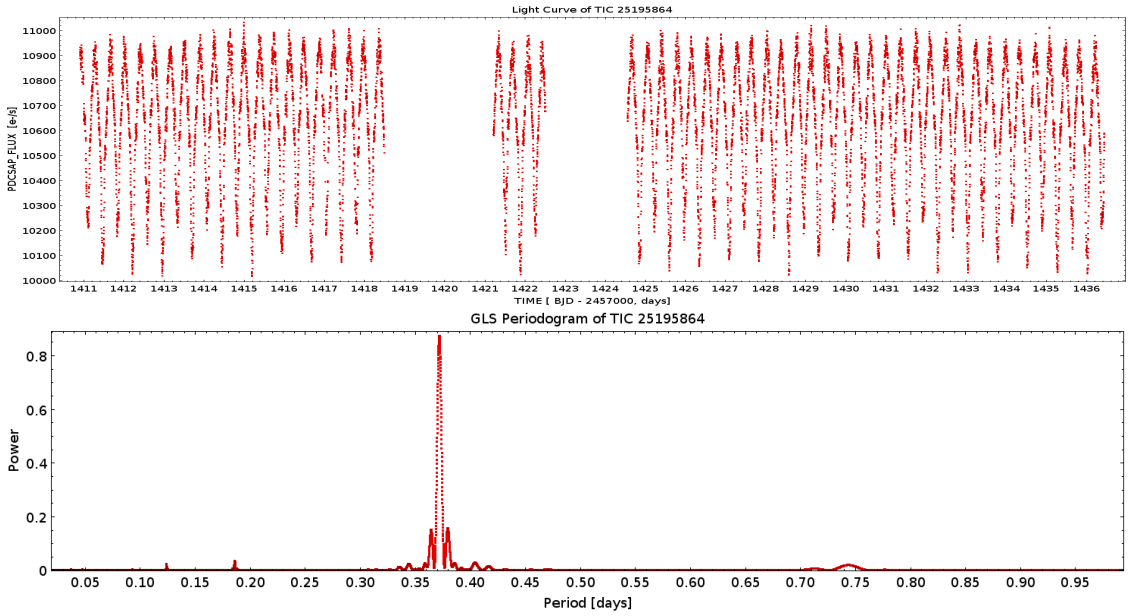


Figure 3.9: One sector (two orbits)r light curve(above) and GLS Periodogram(below) of TIC25195864 (TESS Sector 4) .

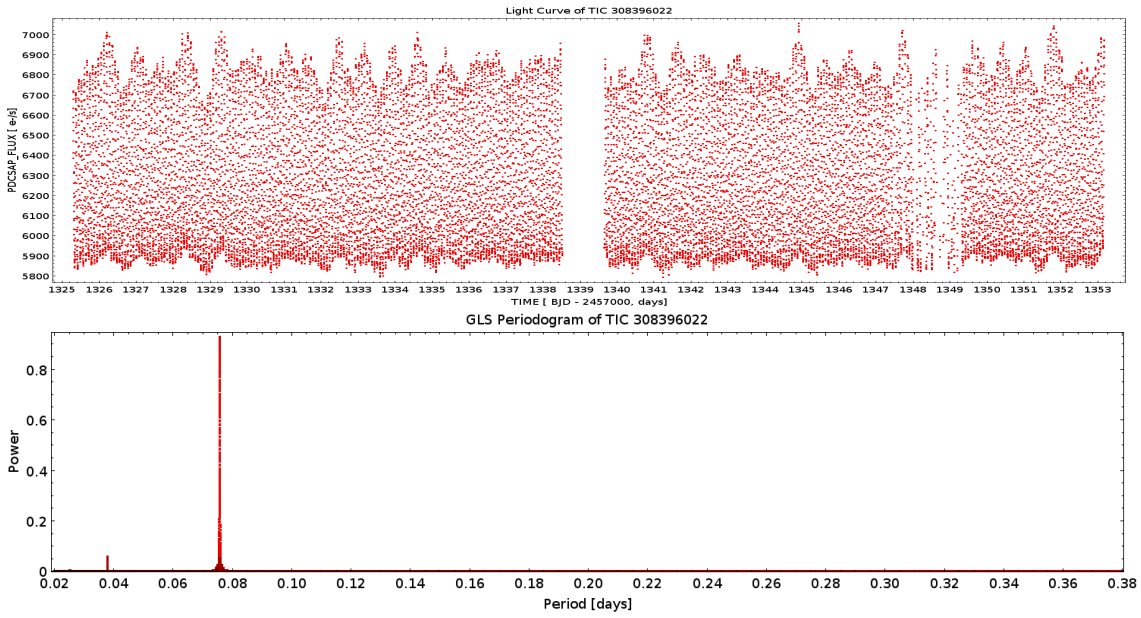


Figure 3.10: One sector (two orbits) light curve(above) and GLS Periodogram(below) of TIC308396022 (TESS Sector 1).

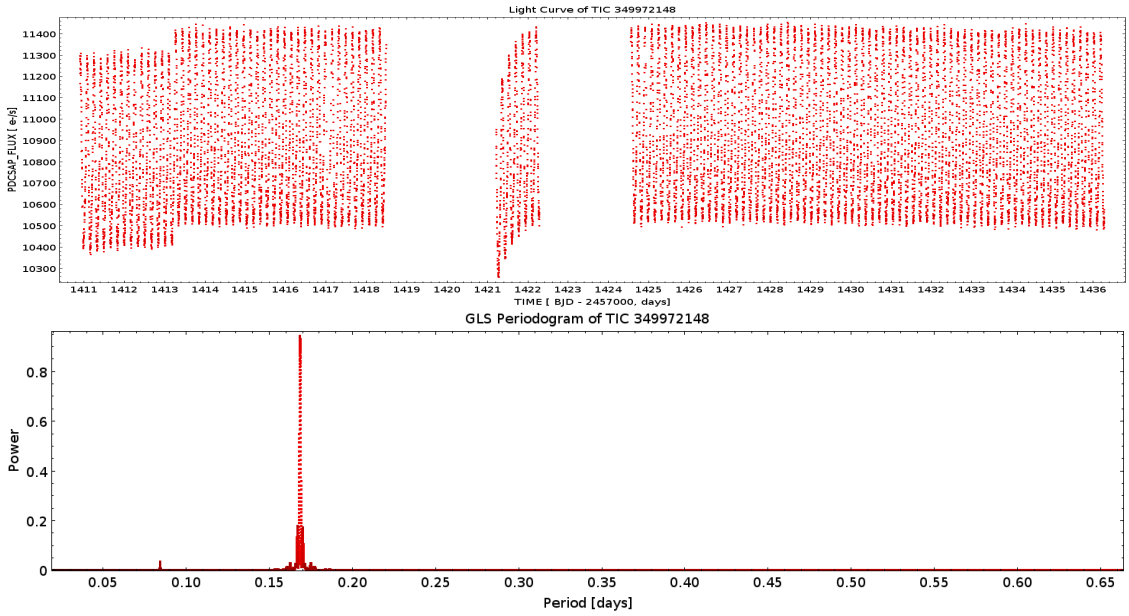


Figure 3.11: One sector (two orbits) light curve(above) and GLS Periodogram(below) of TIC349972148 (TESS Sector 4).

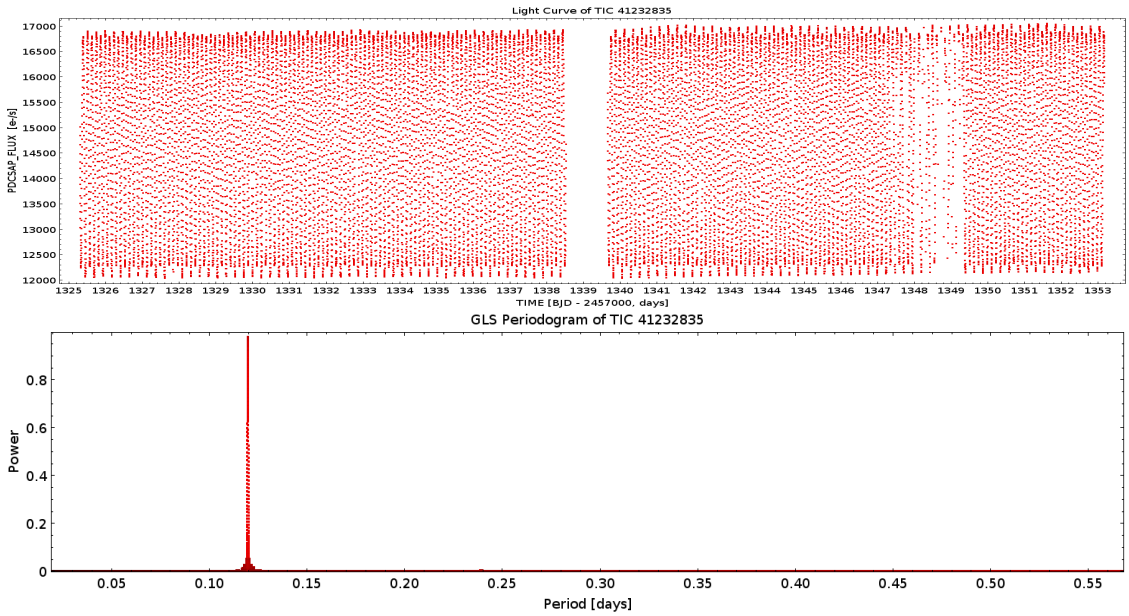


Figure 3.12: One sector (two orbits) light curve(above) and GLS Periodogram(below) of TIC41232835 (TESS Sector 1) .

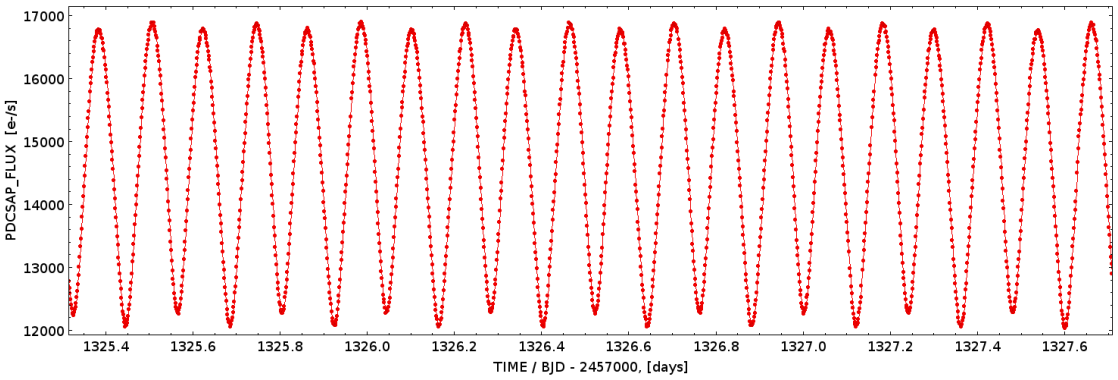


Figure 3.13: A closer look at the light curve of TIC 41232835 (Sector 1) showing an alternate sequence of minima with two different depths.

(0.09294032 days) with the period that is mentioned in the Chang 2013 catalog (0.12 days). However signal with the second highest power from my VARTOOLS analysis matches the Chang 2013 catalog period (0.12 days). This could be due to Chang et al. (2013) catalog calculated periods based on ground-based surveys whereas I have used space-based TESS data which is more accurate.
The initial periodograms of the targets TIC260654645 (Figure 3.4) , TIC364399376 (Figure 3.5) , TIC38515566 (Figure 3.6) which were already analyzed in Vaulato et al. (2022) is being re-analyzed by me. The targets have 6, 5, and 10 more sector data respectively from when previously analyzed. The results give the same single fundamental pulsation mode with which the previous analysis was done. I did not do further analysis on these targets.
Analysis of the initial sectors periodograms of targets TIC 25195864 (Figure 3.9), TIC308396022 (Figure 3.10), TIC349972148 (Figure 3.11) and TIC41232835 (Figure 3.12) I found that all the targets have a strong single pulsation frequency mode. This makes them a good target to continue the PT method. The light curve of TIC34997218 shows a very evident systematic offset on some specific orbits. I took care of this before the harmonic fitting stage. In the literature TIC41232835 (Figure 3.12 is listed as an Eclipsing Binary (Kiraga, 2012). Taking a closer look at the light curve of TIC4123283(Figure 3.13), it can be seen that there is an alternating sequence of minima with two different depths, which clearly shows it to be a contact eclipsing binary (Prša et al., 2022).

The other three targets were used for a more detailed analysis where I downloaded the 2-minute cadence light curves of all sectors from TESS observation. I converted the data from each sector from flux to magnitudes and divided them into orbits, and then merged them using VARTOOLS to form a light curve spanning the entire duration of observations.

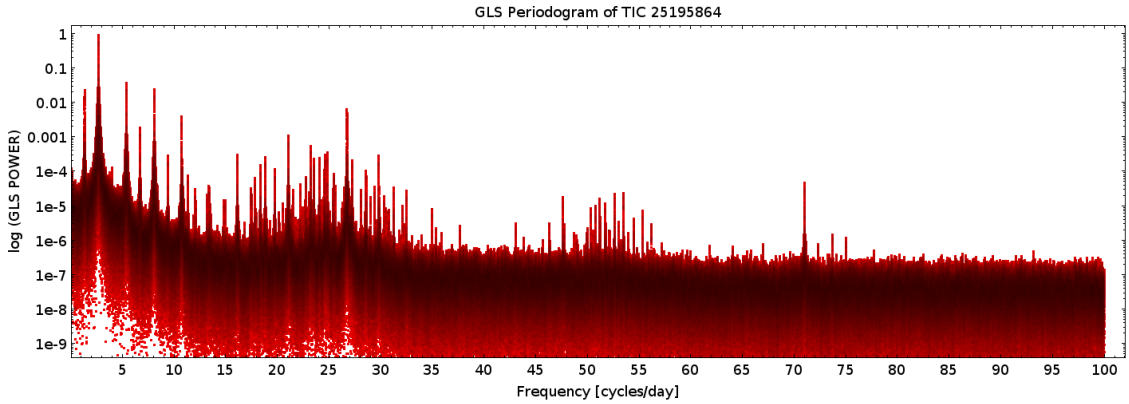


Figure 3.14: Periodogram of TIC 25195864 in GLS Power vs Frequency plot.

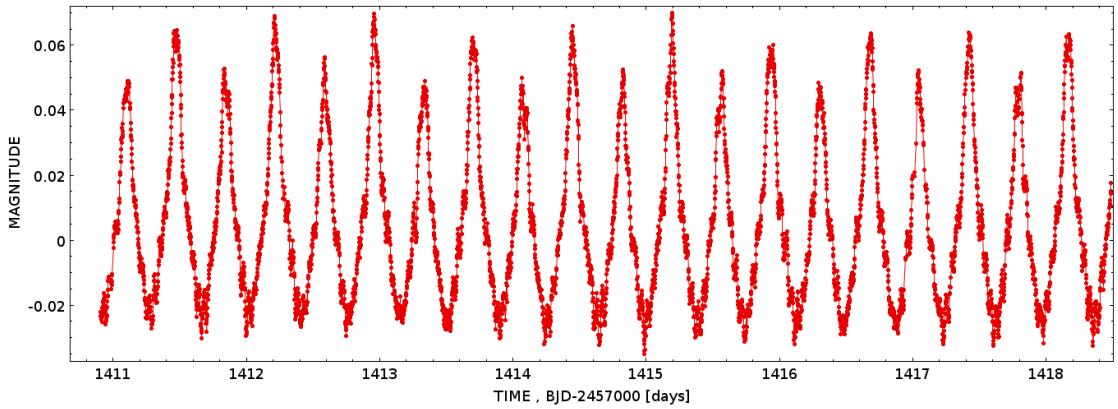


Figure 3.15: Close view of the light curve of TIC 25195864 (TESS Sector 4) showing an alternate sequence of minima with two different depths.

After getting all the orbits data into a single file, I computed the GLS periodogram on the light curve data spanning all sectors as well as each of the single orbits separately. The periodograms of TIC 349972148 (Figure 3.19 ) and TIC 308396022 (Figure 3.24), provided in the next section, have a prominent single pulsation mode. These are ideal results to move to Harmonic analysis described in the next section.

TIC25195864 is clearly a much more complicated case as seen from Figure 3.14. There are at least two pulsation modes in the low-frequency range (0-12 cycles/day) plus a complex forest of peaks at 16-30 cycles/day. This makes the frequency spectrum of the target very chaotic so I did not analyze this target any further. Looking closely at its light curve further shows that the shape of a semi-contact eclipsing binary light curve(Figure 3.15) (Prša et al., 2022).

## 3.3 Harmonic analysis of specific targets

### 3.3.1 Harmonic fit (-killharm)

I have fit a harmonic curve to the light curve with a frequency equal to the fundamental pulsation mode that I got from the GLS periodogram. This was executed with the -killharm command of VARTOOLs program, which fits the required harmonic function to the curve of the form:

$$K(t) = \sum_{i=1}^{Nper} \left( \sum_{k=0}^{Nharm_i} [a_{ik} \sin(2\pi(k+1)f_i t) + b_{ik} \cos(2\pi(k+1)f_i t)] + \sum_{k=0}^{Nsubharm_i} \left[ c_{ik} \sin\left(\frac{2\pi f_i t}{k+1}\right) + d_{ik} \cos\left(\frac{2\pi f_i t}{k+1}\right) \right] \right) \quad (3.1)$$

where $N_{per}$ is the number of period, $N_{harm}$ is the number of higher harmonic corresponding to the integer multiple of the period ( $2 * f_i, 3 * f_i, ..., (N_{harm} + 1) * f_i$ and $N_{subharm}$ is the number of sub-harmonics such as ( $f_i/2, f_i/3, ..., f_i/(N_{harm}+1)$. The constants $a_{ik}, b_{ik}, c_{ik}, d_{ik}$ are coefficients of the trigonometric function which will be the output after the fit. Since we are interested in Delta Scuti stars with single pulsation mode, for our purpose $N_{per} = 1$. I also did not consider the sub-harmonics. After fitting this model form, it removes the function to analyze for the next period in the list.
The command outputs the best-fit parameters of the coefficients from each orbit, along with the period and mean magnitude. I have also used the "outampphase" keyword to get the amplitude and phase of the fundamental frequency as well as the harmonics. This is the mathematical form of the outputs: amplitude is $A_k = \sqrt{a_k^2 + b_k^2}$ and the phases $\phi_k = \arctan(-b_k/a_k)/2\pi$.
Considering the best-fit parameters for the pulsation period of the fundamental mode, if I plot the phase shifts of each orbit which were the outputs of the -killharm command, I will be able to construct a $O - C$ plot of the phase shifts from the fundamental pulsation mode. Using the out put I plotted the phase shifts as a function of time, which gave the rough $O - C$ plot induced by the LTTEs.

The timing drifts can be calculated to be in seconds from the phase shifts using the formula

$$O - C = \frac{(\phi_0 - \phi_{0,mean}) \times P_{dom} \times 86400}{N} \quad (3.2)$$

where $\phi_0$ is the fundamental phase which is returned by the least square fit, $\phi_{0,mean}$ is the mean of the phase shifts across all orbits, $P_{dom}$ is period of the fundamental pulsation mode, $N$ is the number which is assumed to be 1 for the fundamental phase and 86400 is to convert the phase shift from days to seconds.

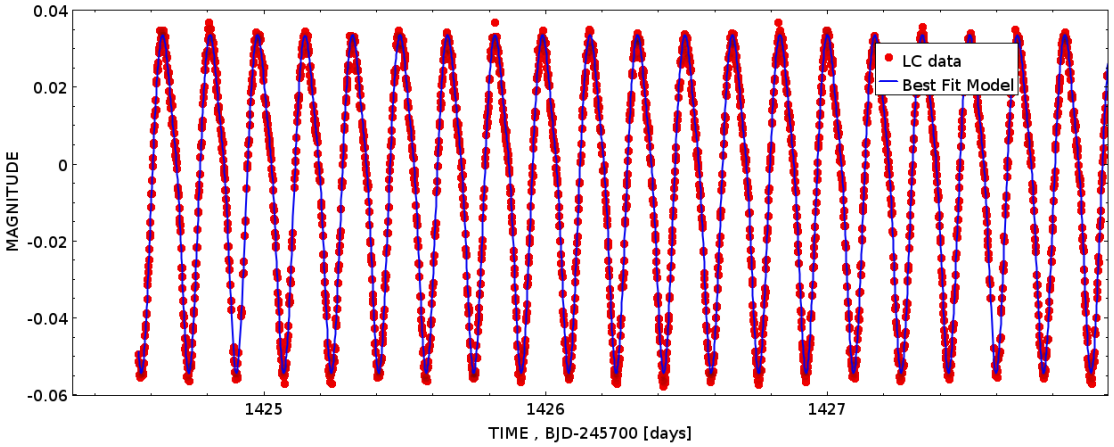


Figure 3.16: The Best-fit model from the killharm command fitted on the light curve data of TIC 349972148.

### 3.3.2 Harmonic fit (MCMC)

The least-square approach is just a simple, preliminary version of the harmonic analysis of the signal, which in our approach is a two-stage process. The least-square stage is computationally less heavy and thus easier to carry out on large amounts of samples. If this pilot study is carried out on a large sample of targets the least square approach saves a lot of computational work. However to get a more accurate measure of the fitting parameters, as a second stage, I have fitted a more complex model including a quadratic baseline as a function of time along with the sum of sinusoidal functions as previously done. The quadratic baseline is to account for the systematic error/trend in TESS photometry over long timescales (weeks) with respect to the pulsation period (days). The model is then fitted to the light curve with a widely used algorithm called the Monte Carlo Markov Chain (MCMC, Speagle (2020)). This is a Bayesian approach. Here we want to assign a degree of belief to the parameters. The degree of belief can be expressed as a probability in Bayesian statistics using the Bayes theorem which states

$$P(x|D) = \frac{P(D|x)P(x)}{P(D)} \tag{3.3}$$

where $x$ is the parameter in question and $D$ is the data. The expression $P(x)$ is called the prior which is the probability of selected parameters of a model, $P(D|x)$ is called the likelihood which is the conditional probability of getting the data given the parameter $x$, $P(D)$ is the evidence which is the probability of the data, and $P(x|D)$ is the posterior.
The posterior is the probability of the model parameters given the data, the likelihood is the probability of observing the data given a set of model parameters, the

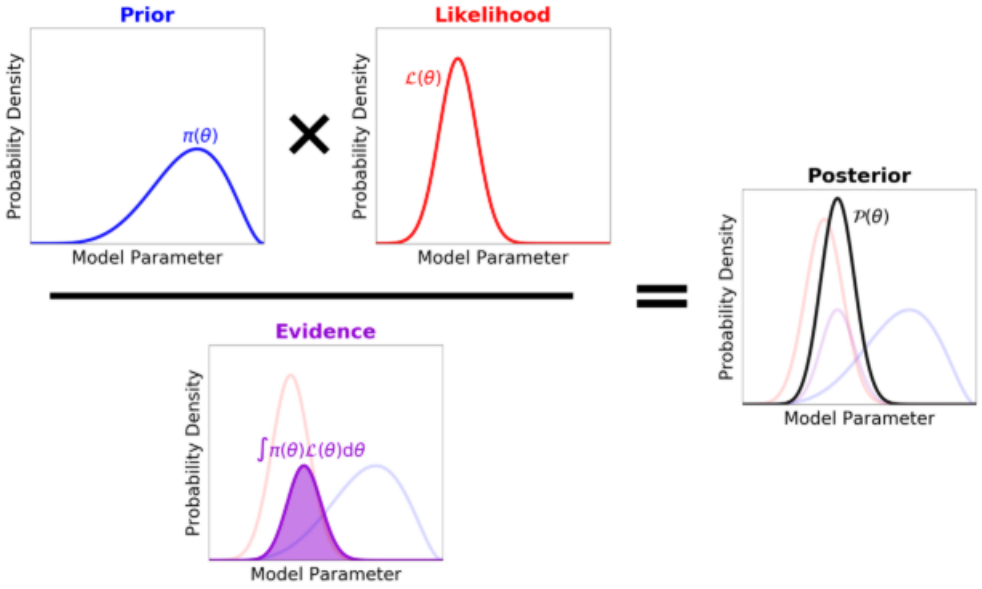


Figure 3.17: Illustration of the Bayes' Theorem. (credit : Speagle (2020))

prior is any previous knowledge of the model parameters and the evidence is the probability of the data. Clearly, if one thing changes here it will affect the overall probability, as expected.

The posterior distribution is usually difficult to determine analytically so we determine it numerically through an MCMC algorithm. This is an approach which uses random sampling to simulate probability distributions and then creates a chain of correlated parameter values over N iterations to compute the posterior probability distribution function defined by Bayes' theorem. A Markov chain is one in which there is no memory of the previous step so it only depends on the current one. The starting points for these chains are very important because a poor starting point will produce a poor representation of the data or get the chains stuck in a local minimum. The starting points or the priors that I am providing are not random, but they are the values that I had previously got from the -killharm fitting of a sinusoidal curve as mentioned in the previous section.
I am using a non-linear model as a function of time which is the only independent parameter. The model has a quadratic and a sinusoidal function in it. The sinusoidal part includes a function for the fundamental node as well as the subsequent

harmonics. The general form of our model is:

$$NL(t) = b_0 + b_1 \cdot (t - t_{median}) + b_2 \cdot (t - t_{median})^2 + A_0 \cdot \cos(\frac{2\pi t}{P_{dominant}} + 2\pi\phi_0) + \sum_{i=1}^{H} A_i \cdot \cos(\frac{2\pi t}{(i+1) \cdot P_{dominant}} + 2\pi\phi_i) \quad (3.4)$$

where $b_0, b_1$ and $b_2$ are the coefficients of the linear and quadratic terms. $A_0$ and $A_i$ are the amplitude of the fundamental mode and higher harmonics respectively. $\phi_0$ and $\phi_i$ are the phases of the fundamental mode and higher harmonics respectively. $P_{dominant}$ is the dominant period of pulsation which has been calculated previously from the GLS periodogram.

The results after the MCMC fit are best-fit values of parameters and their associated error margins computed for each orbit. Considering the best-fit parameter for the pulsation period of the fundamental mode, I plotted the phase shifts of each orbit, thus constructing a $O - C$ plot of the phase shifts from the fundamental pulsation mode. The timing drifts can be calculated to be in seconds from the phase shifts using a formula similar to the previous section.

$$O - C = \frac{(\phi_0 - \phi_{0,mean}) \times P_{dom} \times 86400}{N} \quad (3.5)$$

where $\phi_0$ is the fundamental phase which is returned by the least square fit, $\phi_{0,mean}$ is the mean of the phase shifts across all orbits, $P_{dom}$ is period of the fundamental pulsation mode, $N$ is the number which is assumed to be 1 for the fundamental phase and 86400 is to convert the phase shift from days to seconds.

The MCMC fit providing more accurate results of parameters and also calculating the uncertainties on each of them is definitely a more reliable method for this analysis when compared with the least square approach. In the next section, I have shown the results of the MCMC approach and also used it later for fitting model functions to the residuals of $O - C$ plot after accounting for long-term and systematic trends.

### TIC 349972148 / Chang 414

Chang 414 is a single pulsation Delta Scuti star, with an estimated mass of 2.15 ± 0.10 $M_\odot$. It was observed by TESS continuously for 10 sectors, (Sector 4, 5, 6, 7, 8, 9, 10, 11, 12, and 13) starting from 19th October 2018 to 18th July 2019. The light curve had some systematic errors in the first orbit of the first sector which I had to discard for further analysis. I extracted a periodogram on the all-sector light curve (Figure 3.19 with a range from 0.01 to 28 days with a step size of 0.01 days. The result gives a fundamental pulsation period at $P_{dominant}$ = 0.16852 days and also

gives 3 subsequent harmonics which are in fact integer multiples of the fundamental pulsation mode.

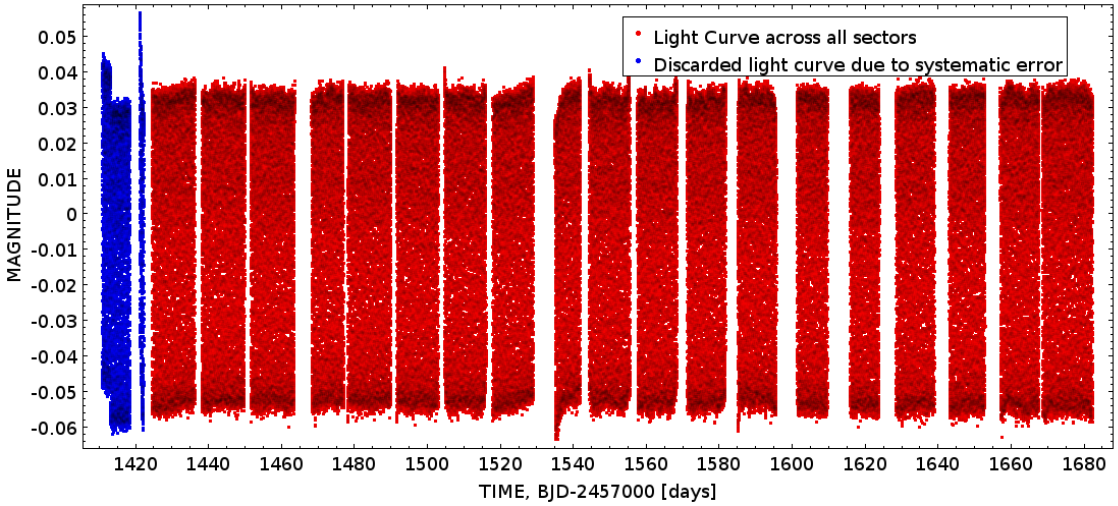


Figure 3.18: All sector light curve of TIC 349972148. The blue part of the light curve has been discarded.

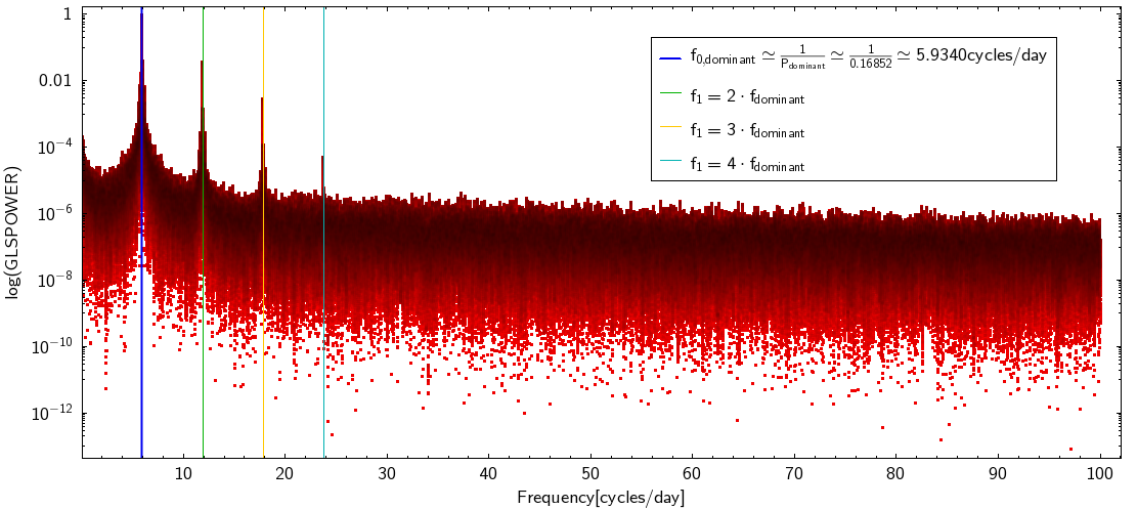


Figure 3.19: Peridogram of the all sector light curve of TIC 349972148. The blue vertical line denotes the fundamental frequency and the other colored lines indicate the subsequent harmonics.

I ran an initial least square fit to check and get a rough estimate of the $O-C$ plot of phase shifts.

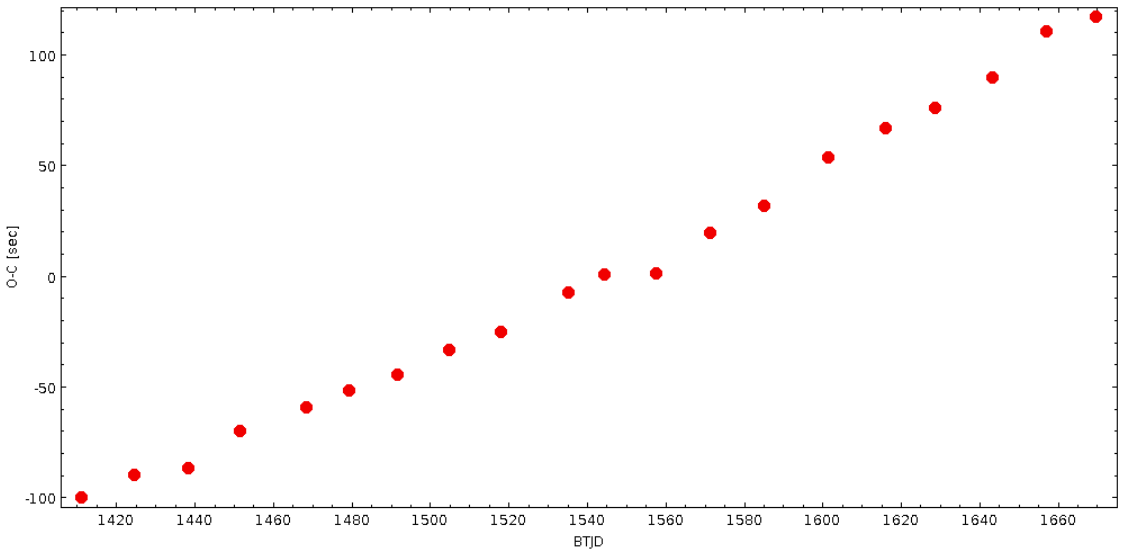


Figure 3.20: O-C plot of TIC 349972148 using the period output of all orbit (0.16852 d). This plot is fitted using the -killharm model.

The figure 3.20 shows a linear trend which in fact has no physical significance, as from Equation 1.3 we see that the linear term only depends on the overall uncertainty in the pulsation period. Only the second derivative of the phase shift matters here. So the linear trend made evident that the period used to fit the curve was not accurate enough. So I ran another periodogram on all the orbit light curves by setting a smaller period range between 0.168 and 0.169 days, and with a smaller step size of 0.0005 instead of 1. This resulted in a more accurate determination of the period having more significant figures. ($P_{dominant} = 0.16852027$). 3.21 I used this more accurate period to fit another killharm model and a nonlinear fit of the MCMC model to get the $O - C$ plot. The result is shown in Figure 3.22

The $O-C$ diagram shows the difference between the phase shift that is observed from the TESS light curve and the calculated ones from the model fit with the fundamental mode. The plot here contains 20 points, one from each orbit from all the observed sectors (10 sectors). Since the MCMC model is more accurate, I will use the phase shift model from MCMC for further analysis. I have plotted it as a deviation from the mean phase that I got from the fitted model. It can be seen that there is a deviation from the mean phase which could be due to the LTTE. To analyze the origin of this deviation and relate it to the LTTE, I have done an order of magnitude analysis of LTTE signals that may arise on Chang 414 due to a secondary perturber.

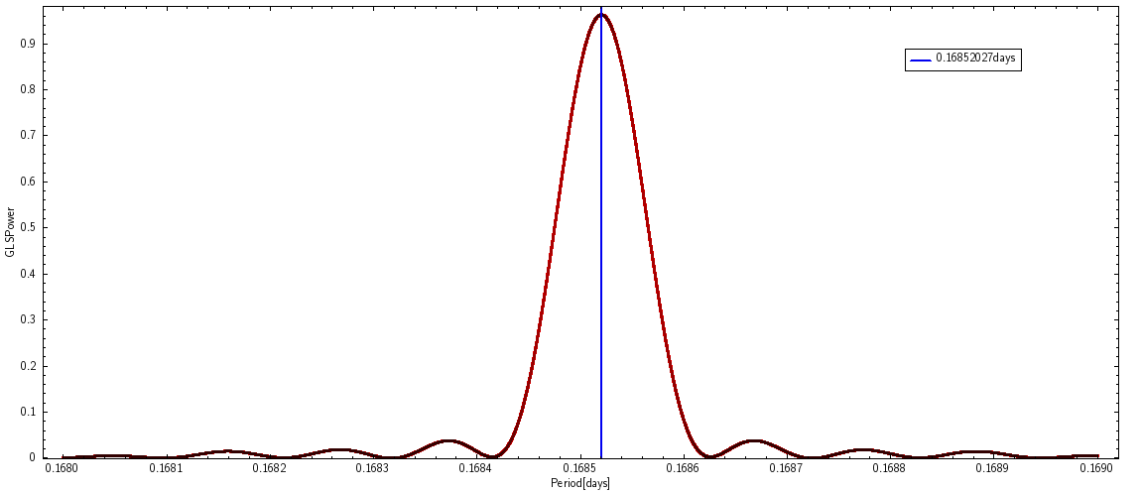


Figure 3.21: Accurate periodogram around the fundamental pulsation period of Chang 414.

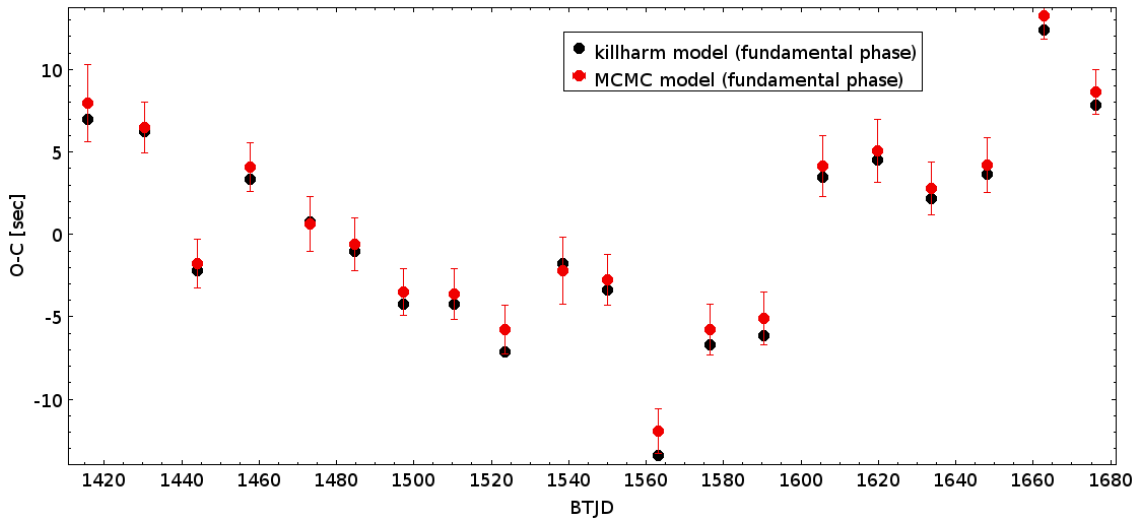


Figure 3.22: The $O-C$ plot of Chang414. The black points are from the killharm model in Section 3.3.1, and the red points with error bar are from MCMC model as mentioned in Section 3.3.2

### TIC 308396022/Chang 451

TIC 308396022 is a Delta Scuti star having an estimated mass of 1.50 $M_{\odot}\pm$ 0.13, having a TESS magnitude of 11.07. It was observed by TESS for 22 sectors (1, 4, 5, 7, 8, 9, 10, 11, 27, 28, 31, 34, 35, 37, 38, 61, 62, 63, 64, 65, 68, 69) from 25th July 2018 to 20th September 2020.

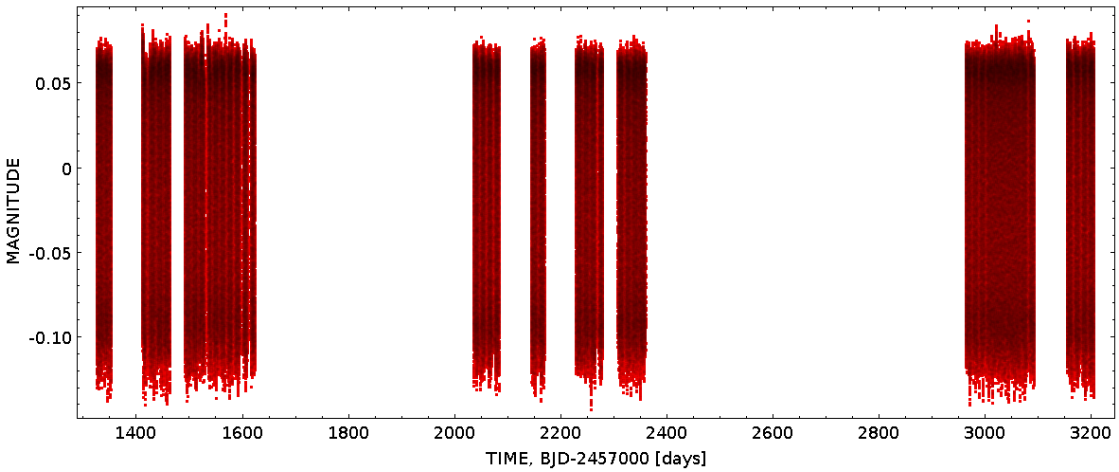


Figure 3.23: Light curve of TIC 308396022 (all TESS sectors).

I ran a similar periodogram on the merged light curve from all sectors, searching for periods between 0.01 to 28 days, having a step size of 0.01 days. Analyzing the spectral frequency pattern of Chang 451, from the logarithmic periodogram, it is evident that it has a main fundamental pulsation mode with $P_{dominant} = 0.07574$ days, and gives 5 subsequent harmonics which are integer multiples of the fundamental mode. There are some additional frequencies at ∼6 and ∼19 cycles/day but their power is negligible when compared to the main series, so for this analysis I just considered the main pulsation mode and two harmonics.

For a more accurate measurement, I ran the periodogram close to the rough estimated pulsation period I got from the previous analysis and found the fundamental pulsation period to be $P_{dominant} = 0.07573677$ days.

With the estimation of the accurate fundamental frequency, I set up the basic harmonic model as described in the section of -killharm and a non-linear fit function using the MCMC model. As seen from Figure 3.26 both models are in well accordance with each other. The $O - C$ plot shows the difference in phase shift between the observed light curve and the calculated median phase shift from the model fits. The plot is made of 44 data points, one from each orbit of the observed light curve of 22 sectors. It can be seen from Figure 3.26 that there is a deviation from the median phase and the change in phase shift is approximately sinusoidal. This shows the presence of another companion which causes this periodic change in the phase shift of Chang 451.

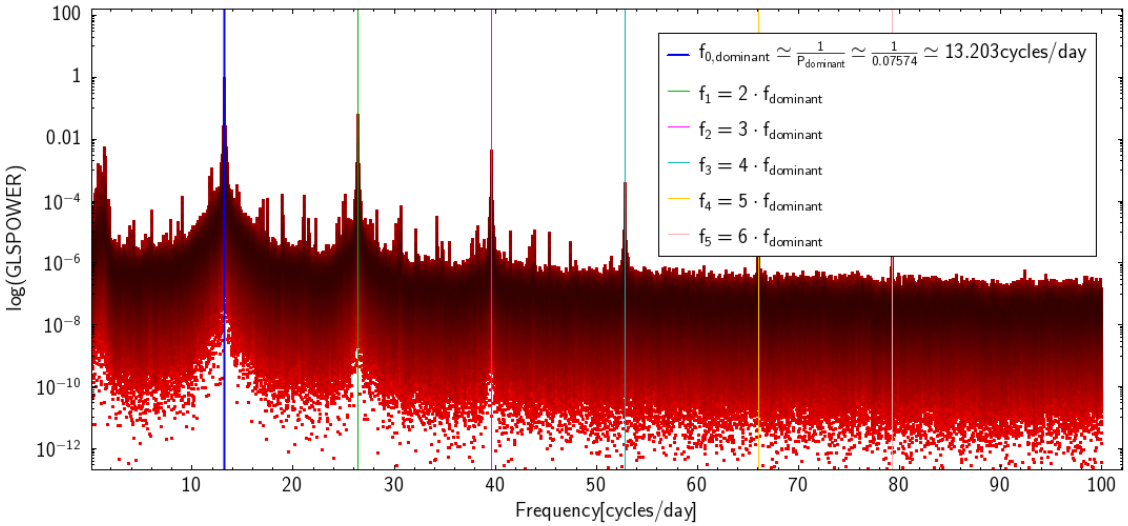


Figure 3.24: Periodogram of the all-sector light curve of TIC 308396022. The blue vertical line denotes the fundamental frequency and the other colored lines indicate the subsequent harmonics.

### 3.3.3 Computation of expected LTTE signal

To understand the origin of the signal that I observed from the $O - C$ plot, it is crucial to check the order of magnitude of the LTTE signal originating due to the presence of a secondary companion. For this, I calculated for each of the two targets, the expected semi-amplitude of the LTTE signal as a function of the orbital period and semi-major axis of the companion body. This also aids in determining the parameter space of the companions that we can detect using the PT technique. Thus, using this technique and observing the phase shift signal we get an idea of the mass, semi-major axis, and orbital period of the secondary companion.

For each mass value of the companion, I have assumed a range of mass. The mass range with the name of the companions are taken from Stevens and Gaudi (2013). I have also calculated the mean mass of the ranges to use in the calculation later.

Assuming a circular orbit and setting the inclination angle to be $90^o$, and using it in the equation 1.1, I calculated the semi-amplitude of the expected LTTE signal, A in units of seconds, as a function of the semi-major axis taken from 0 to 10 A.U. I have also calculated the corresponding orbital period based on Kepler's equation,

$$P_{orb} = 2\pi a \cdot \sqrt{\frac{a}{GM_\star}} \tag{3.6}$$

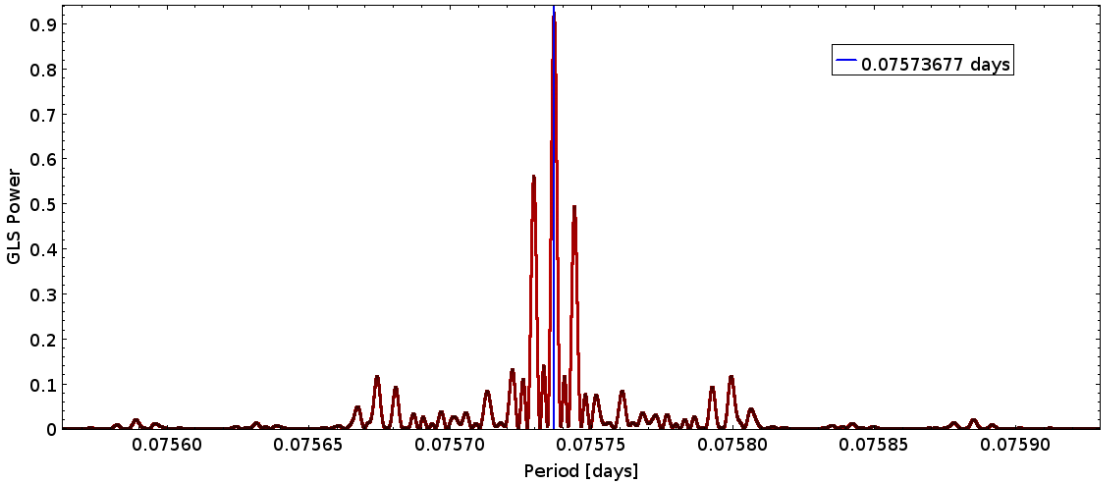


Figure 3.25: Accurate Periodogram around the fundamental pulsation period of Chang 451.

| Perturber | Mass Range | Mean Mass $[M_\oplus]$ |
|---|---|---|
| Earth | 0.1 $[M_\oplus]$ - 2 $[M_\oplus]$ | 1.0 |
| Super Earth | 2 $[M_\oplus]$ - 10 $[M_\oplus]$ | 6.0 |
| Neptune | 10 $[M_\oplus]$- 100 $[M_\oplus]$ | 55.0 |
| Jupiter | 100 $[M_\oplus]$ - $10^3$ $[M_\oplus]$ | 550.0 |
| Brown-dwarf | 13 $[M_J]$ - 0.07 $[M_\odot]$ | 13720.0 |
| Solar | 1 $[M_\odot]$ | 333030.0 |

Table 3.3: Approximated ranges of perturbing masses.

where $G = 8.88 \times 10^{-10} AU^3/M_\oplus \text{days}^2$ being the universal gravitational constant expressed in the appropriate units for the current calculation, a is the semi-major axis taken with a step size of 0.1 A.U. from 0 to 10 AU, $M_\star$ is the mass of the pulsating star expressed in units of $M_\oplus$. The masses of the target Chang 414 and Chang 451 are taken from the StarHorse2 Catalog (Anders et al., 2022).

**Chang 414**

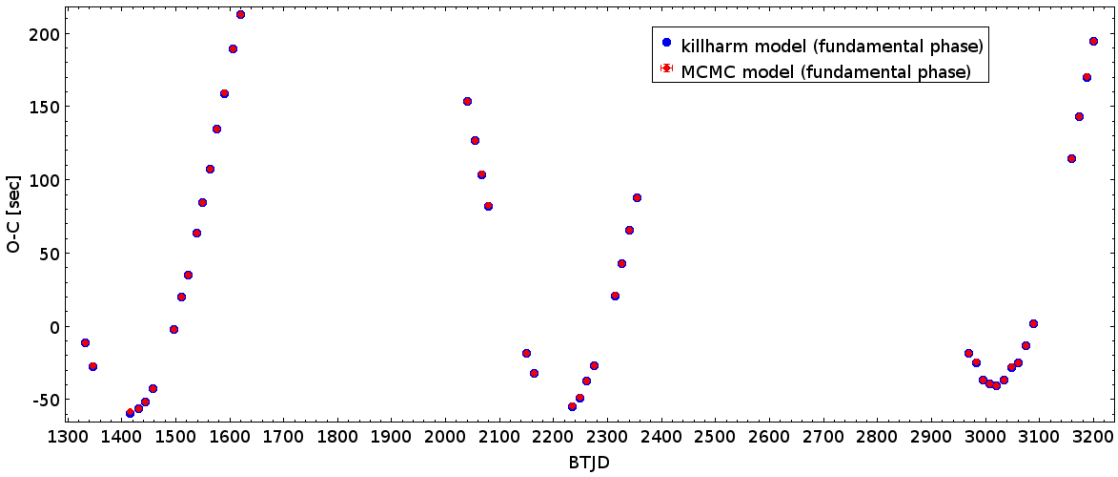


Figure 3.26: The $O-C$ plot of Chang451. The blue points are from the killharm model in Section 3.3.1, and the red points with the error bar are from the MCMC model as mentioned in Section 3.3.2

| Perturber | Mass [$M_\oplus$] | A(a) [AU·sec] |
|---|---|---|
| Earth-like | 1.0 | 0.00100·.$a$ |
| Super Earth-like | 6.0 | 0.006009·.$a$ |
| Neptune-like | 55.0 | 0.055084·.$a$ |
| Jupiter-like | 550.0 | 0.550835·.$a$ |
| Brown dwarf-like | 13720.0 | 13.7408·.$a$ |
| Solar-like | 333030.0 | 333.536·.$a$ |

Table 3.4: LTTE signal produced by Chang 414 as a function of semi-major axis.

**Chang 451**

| Perturber | Mass [$M_\oplus$] | A(a) [AU·sec] |
|---|---|---|
| Earth-like | 1.0 | 0.000695·.$a$ |
| Super Earth-like | 6.0 | 0.004171·.$a$ |
| Neptune-like | 55.0 | 0.038232·.$a$ |
| Jupiter-like | 550.0 | 0.382319·.$a$ |
| Brown dwarf-like | 13720.0 | 9.53712·.$a$ |
| Solar-like | 333030.0 | 231.498·.$a$ |

Table 3.5: LTTE signal produced by Chang 451 as a function of semi-major axis.

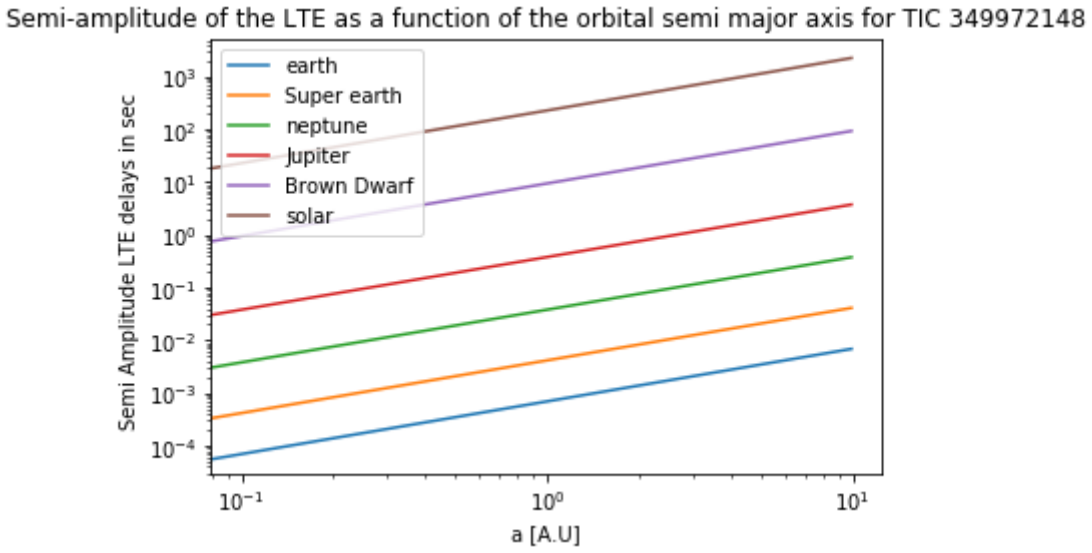


Figure 3.27: Semi-amplitude of the LTTE as a function of the orbital semi-major axis varying in the interval 0-10 AU, both axis are in logarithmic scales. Each color refers to a different companion orbiting Chang 414.

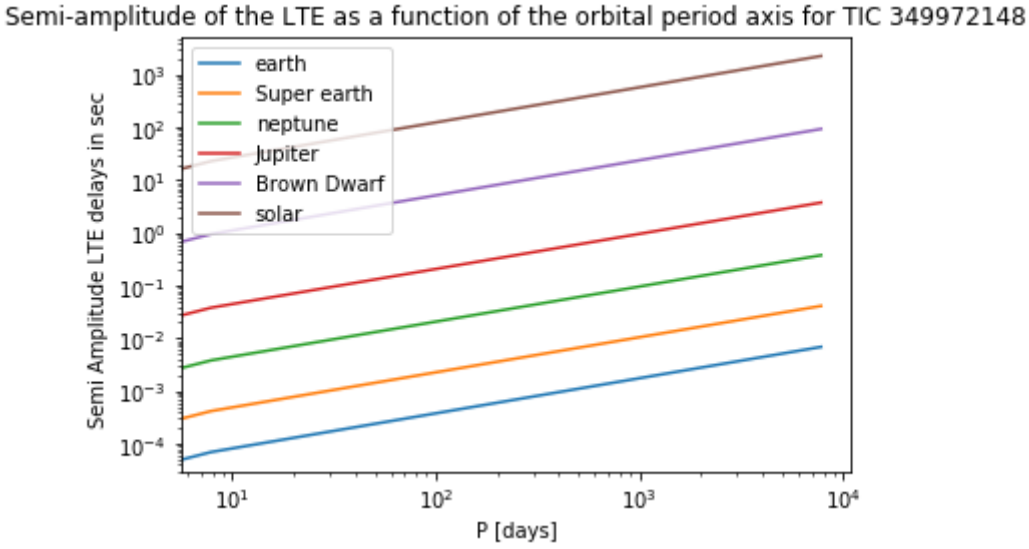


Figure 3.28: Semi-amplitude of the LTTE as a function of the orbital period assuming a semi-major axis varying in the interval 0-10 AU, both axis are in logarithmic scales. Each color refers to a different companion orbiting Chang 414.

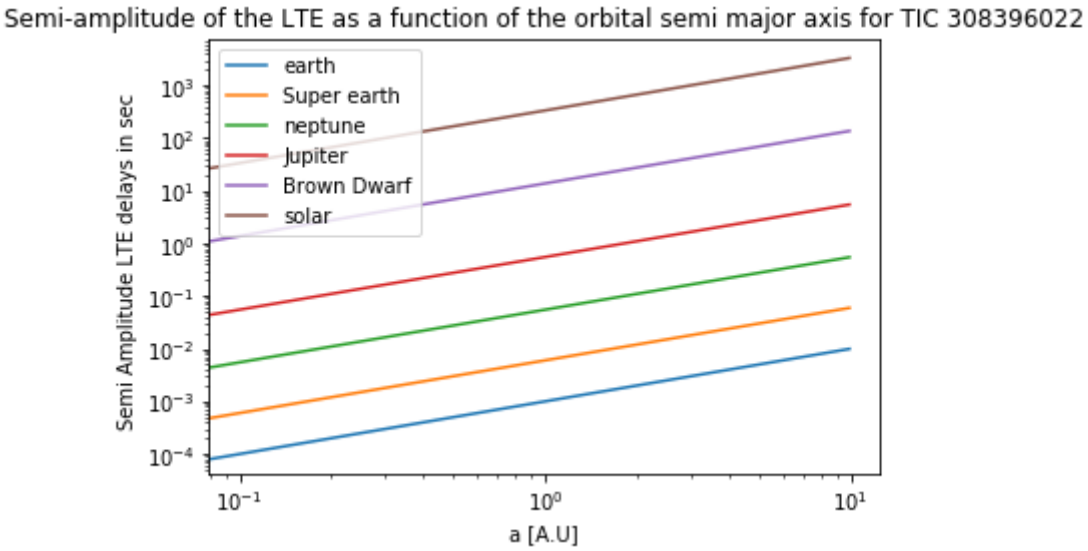


Figure 3.29: Semi-amplitude of the LTTE as a function of the orbital semi-major axis varying in the interval 0-10 AU, both axis are in logarithmic scales. Each color refers to a different companion orbiting Chang 451.

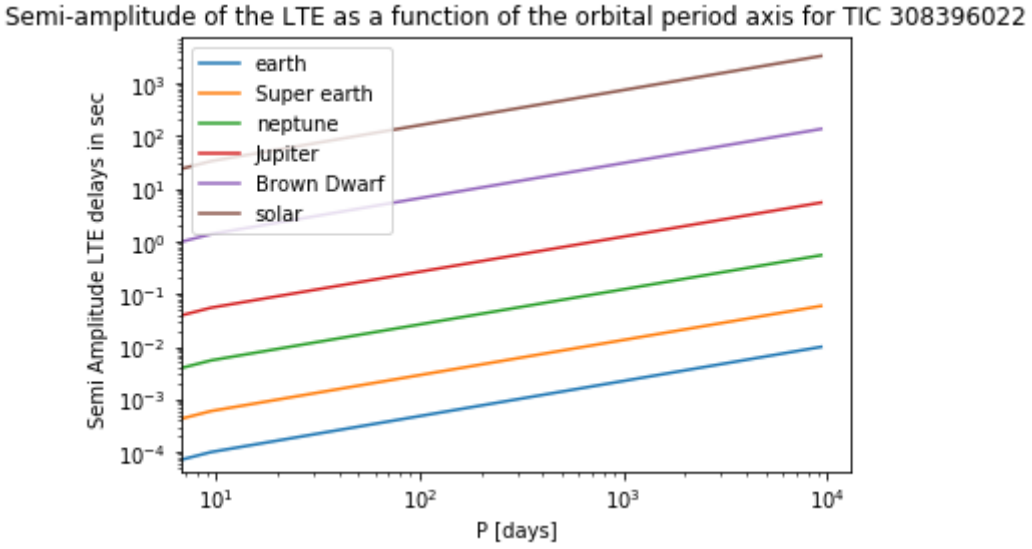


Figure 3.30: Semi-amplitude of the LTTE as a function of the orbital period assuming a semi-major axis varying in the interval 0-10 AU, both axis are in logarithmic scales. Each color refers to a different companion orbiting Chang 451.

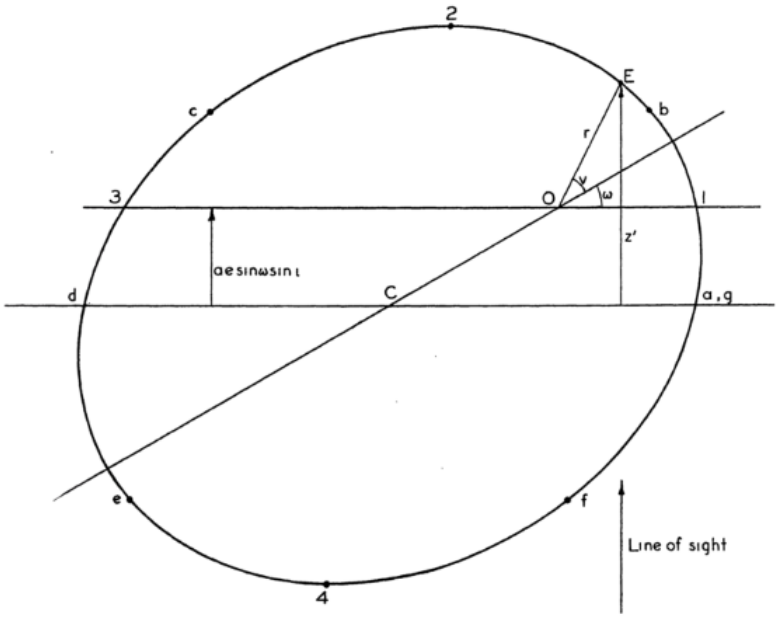


Figure 3.31: In this model E is the orbital position of the secondary component of an eclipsing binary system, as investigated by John B. Irwin in its review. The segment dCa is the intersection of the orbital plane and the tangent plane passing through the center of the ellipse. For convenience, $i = 90^o$ is assumed. Image credit: Irwin (1952)

## Note

As theoretically seen in Equation 1.1, for a simple circular orbit, with a more massive perturber and greater semi-major axis of the perturber, we get a greater LTTE semi-amplitude signal.

In the general case of an eccentric orbit, the equation for semi-amplitude of the time delay (Irwin, 1952) depends on the eccentricity as

$$A \propto \frac{a \sin i \cdot \sqrt{1 - e^2 \cos^2 \omega}}{c} \tag{3.7}$$

where $A$ is the semi-amplitude of the light-time travel delay, $i$ is the inclination angle of the orbit, $a$ is the semi-major axis,$e$ is the eccentricity of the orbit, $\omega$ is the argument of periapsis and c is the speed of light.(Figure 3.31) Assuming fixed values for $i = 90^o$ and $\omega = 0^o$, Equation 3.7 shows a decrease in the semi-amplitude signal of LTT with an increase in eccentricity.

# Chapter 4

# Results

In this chapter, I will describe the final procedure to fit the LTTE signal from the $O-C$ diagram, after adding a polynomial baseline to our model to account for trends due to long-period perturbers. The results and interpretation from this analysis are also presented. Lastly, I will discuss the problems with TESS timing accuracy and future developments that can be done to improve the Pulsation Timing method.

## 4.1 O-C plot fitting

Before performing a sinusoidal fit to the $O-C$ plot, it is necessary to de-trend the plot from any linear or quadratic trends. The linear trend is just an artifact, due to the inaccurate choice of average pulsation period and the quadratic trend could be due to a perturber on an extremely large orbit, for instance, a distant stellar companion. For this I had to fit the required functions suitable for each target and then plot the residuals. Ultimately I have performed a GLS periodogram on the residuals to determine any possible periodic variation that exists due to a secondary companion. In the last step, I performed a non-linear fit of a harmonic function using the same MCMC model, based on the period value I got from the periodogram, to find how well this value fits. I used the best-fit values and its errors returned by the MCMC fit to constrain the orbital semi-major axis (in AU) and the possible mass of the perturbing companion (in $M_{\oplus}$). The equation to calculate the semi-major axis is

$$a = \left( \frac{P_{orb}^2 \cdot G \cdot M_{\star}}{4\pi^2} \right)^{1/3} \tag{4.1}$$

where $G = 8.88 \times 10^{-10} AU^3/M_{\oplus}$ days$^2$ being the universal gravitational constant expressed in the appropriate units for the current calculation, $a$ is the semi-major axis, $M_{\star}$ is the mass of the pulsating star expressed in units of $M_{\oplus}$. The equation

| Parameter | Best Fit Value | Error |
|---|---|---|
| $a_0$ | -5.29 | 0.58 |
| $a_1$ | 0.0087 | 0.0064 |
| $a_2$ | 0.000926 | 0.000086 |

Table 4.1: Best-fit value for the quadratic trend of the $O-C$ plot of Chang 414.

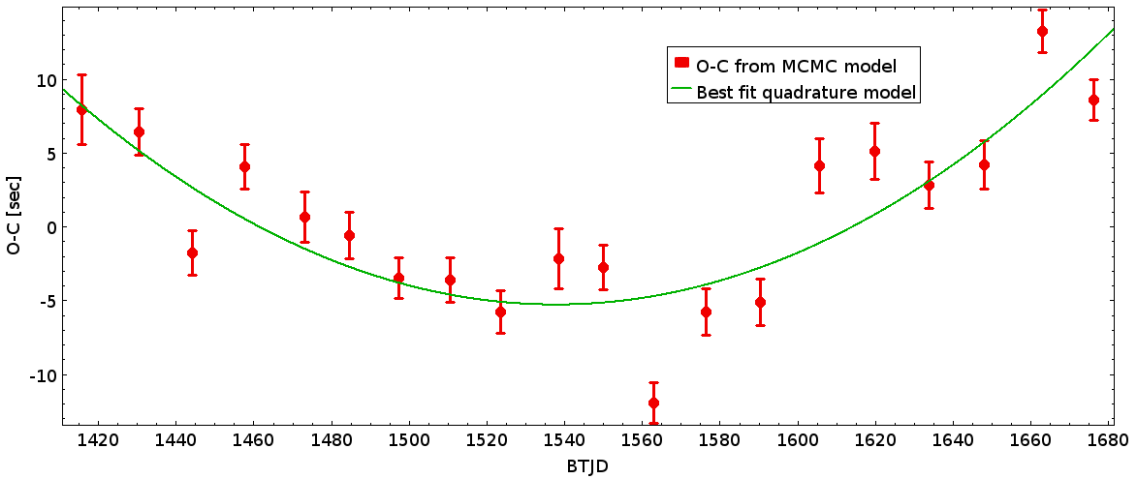


Figure 4.1: Quadratic trend fit on the $O-C$ plot of Chang 414.

for calculating mass is

$$M_p = \frac{c \cdot M_\star \cdot A}{a} \tag{4.2}$$

where $c$ is the speed of light in AU/sec, $M_\star$ is the mass of the pulsating star expressed in units of $M_\oplus$, $a$ is the orbital semi-major axis determined by equation 4.1 and $A$ is the amplitude which corresponds to the RMS value of the signal.

### 4.1.1 TIC 349972148 / Chang 414

From the $O-C$ plot, first I fit a linear and a quadratic function using MCMC to de-trend the plot. The form of the quadratic function is :

$$Q(t) = a_0 + a_1(t - t_{median}) + a_2(t - t_{median})^2 \tag{4.3}$$

where $a_0, a_1$ and $a_2$ are the coefficients of the function.

Subtracting the quadratic trend from the $O-C$ plot, I get the residuals plot. I ran a periodogram on the residual plot, to find any periodic signal that it might detect. The range of period detection I set was 28 days to 400 days. The minimum period is taken 28 days as each orbit data is of 14days, thus we cannot find a period

| Parameter | Best Fit value $\pm\sigma$ |
|---|---|
| $b_0$ | 0.10 ± 0.59 |
| $b_1$ | 0.001423 ± 0.006064 |
| $b_2$ | 4.09406e-06 ± 8.45580e-05 |
| $A_0$ | -2.63 ± 1.24 |
| $P_{orb}$ | 39.13 ± 0.60 days |
| $a$ [AU]$^{\alpha}$ | 0.2913± 0.0055 |
| $M_p$ $[M_J]^{\beta}$ | 40.88 ± 19.45 |

Table 4.2: Best fit value for the harmonic fit in the $O-C$ plot of Chang 414 and other derived parameters of secondary companion.
*$\alpha$ : Calculated using Equation 4.1*
*$\beta$: Calculated using Equation 4.2*

less than that. As reported in Figure 4.2 there is a strong signal at period 39.16501 days. I used this value as a prior to fit a harmonic function (Equation 4.4), using the MCMC model, to the residual $O-C$ plot. Figure 4.3 shows the residual $O-C$ plot and the Best-fit harmonic model that could describe the LTTE on the star due to a secondary compound.

$$NL(t) = b_0 + b_1(t - t_{median}) + b_2(t - t_{median})^2 + A_0 \cdot \cos\left(\frac{2\pi t}{P_{orb} + 2\pi\phi_0}\right) \quad (4.4)$$

where $b_0, b_1$ and $b_2$ are coefficients any remaining quadratic trend, $A_0$ is the amplitude of the harmonic fit, $P_{orb}$ is the orbital period and $\phi_0$ is the phase. The reduced $\chi^2$ for this fit is 2.95322.

From the above fit results and the plots, I concluded that the model is appropriate for the derivation of the required parameters. I got the results of the orbital period, semi-major axis, and the minimum mass. Using the RMS value of the residual signals, I plotted it in the Semi-amplitude variation vs orbital period and Semi-amplitude variation vs orbital semi-major axis, to see the sensitivity until which we can surely discard the presence of any other perturbing companions. The RMS value of the residuals is 3.15 sec which shows that the residual plot is mostly noise as we cannot trust phase shift values of orders of a few seconds, due to the TESS timing inaccuracies.(Discussed in Section 4.2)

My inference from Figure 4.4 and Figure 4.5 is that I can definitely exclude perturbers of mass Brown dwarfs and above having period greater than 200 days for TIC349972148. Also since the data for TIC349972148 spans approximately 260 days, I cannot detect secondary companions with a period of more than 260 days.

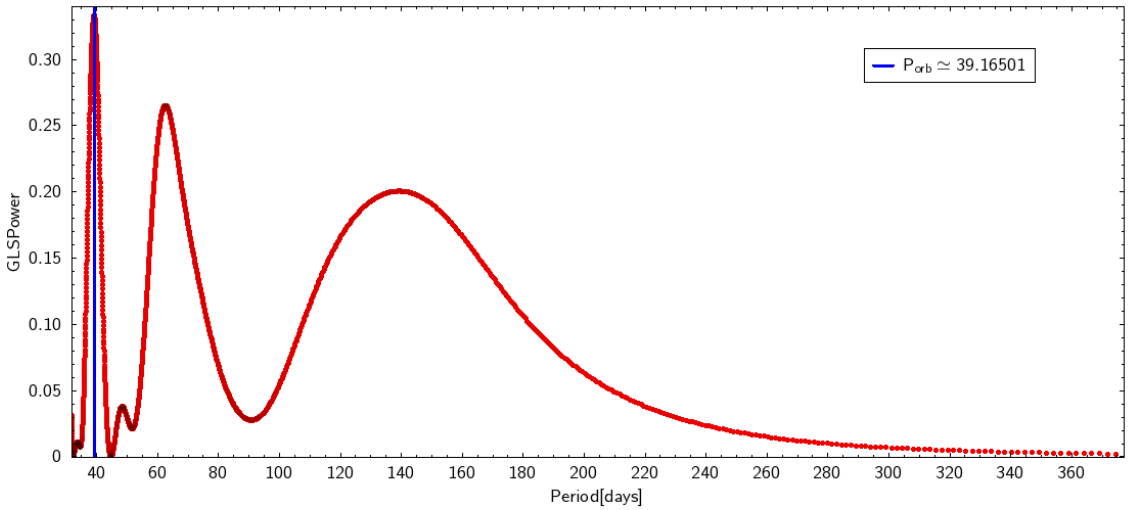


Figure 4.2: Periodogram performed on the residual plot from $O - C$ diagram of Chang 414, after de-trending it for the quadratic trend. The blue line indicates the highest-power signal computed by the GLS Periodogram.

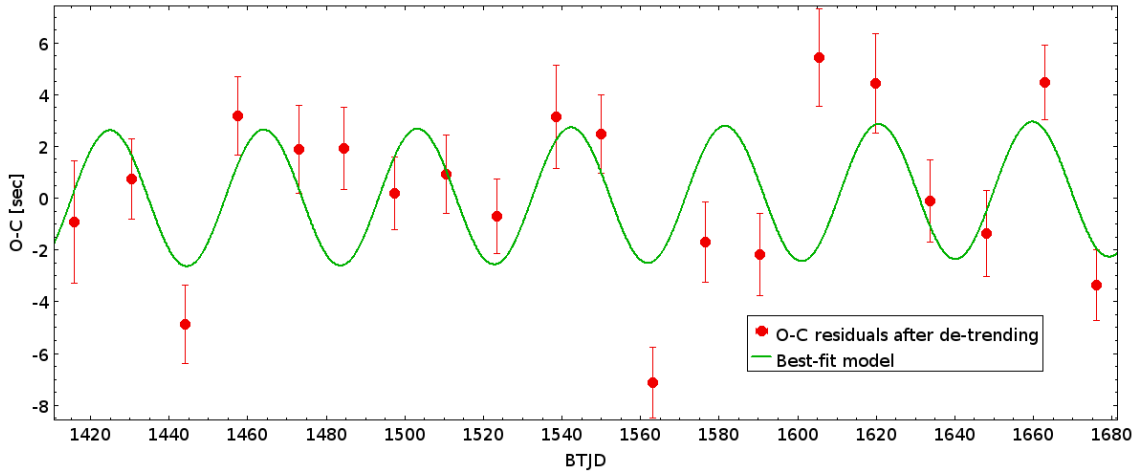


Figure 4.3: Residuals from the $O - C$ plot of Chang 414 after subtracting the quadrature trend. In green the best fit harmonic model is shown having the period taken from Table 4.2.

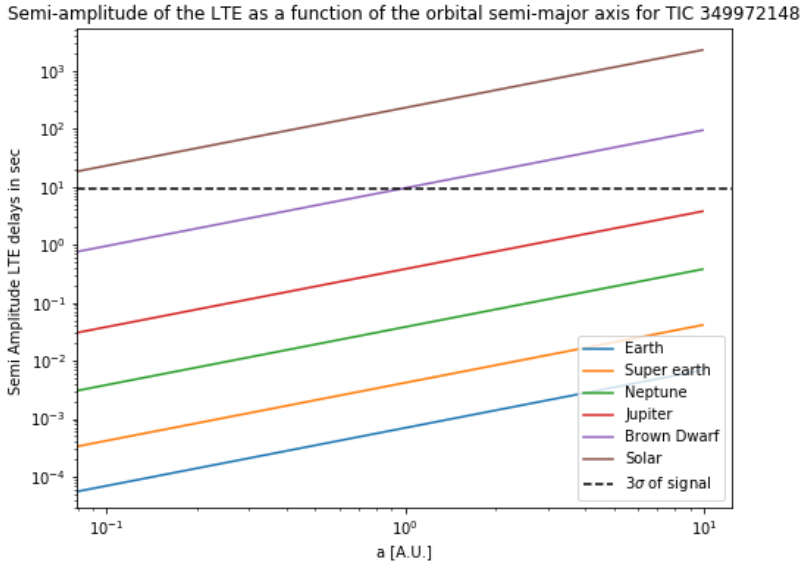


Figure 4.4: The $3\sigma$ of the RMS value of the residuals from Figure 4.3 showing the limits of detection sensitivity of orbital semi-major axis of a secondary companion of Chang 414.

### 4.1.2 TIC 308396022 / Chang 451

The $O-C$ plot of Chang 451 shows a sinusoidal signal which is due to the light travel effect of a secondary companion. I have fit a non-linear function to the $O-C$ plot (Figure 4.6), of the form

$$NL(t) = a_0 + a_1(t - t_{median}) + a_2(t - t_{median})^2 + A_0 \cdot \cos\left(\frac{2\pi t}{P_{orb} + 2\pi\phi_0}\right) \quad (4.5)$$

here $a_0, a_1$ and $a_2$ are coefficients any remaining quadratic trend, $A_0$ is the amplitude of the harmonic fit, $P_{orb}$ is the orbital period and $\phi_0$ is the phase. The resulting parameters from the non-linear fit using the MCMC algorithm is

Calculating the orbital semi-major axis of the using Equation 4.1, I got $a = 1.934 \pm 0.056$ AU, and calculating the companion mass using Equation 4.2, I got $M_c = 0.412 \pm 0.038\ M_\odot$. This secondary companion around TIC 308396022 has also been found by Yang et al. (2021). They used TESS light curve data till sector 38 whereas I used extra 7 sectors of data in my analysis. They calculated the phase shift using the variation of light maximum times of the fundamental mode. A comparison of the orbital parameters found by Yang 2021 and mine is given in Table 4.4. In my analysis, the error bars are improved as I have done the analysis with more data

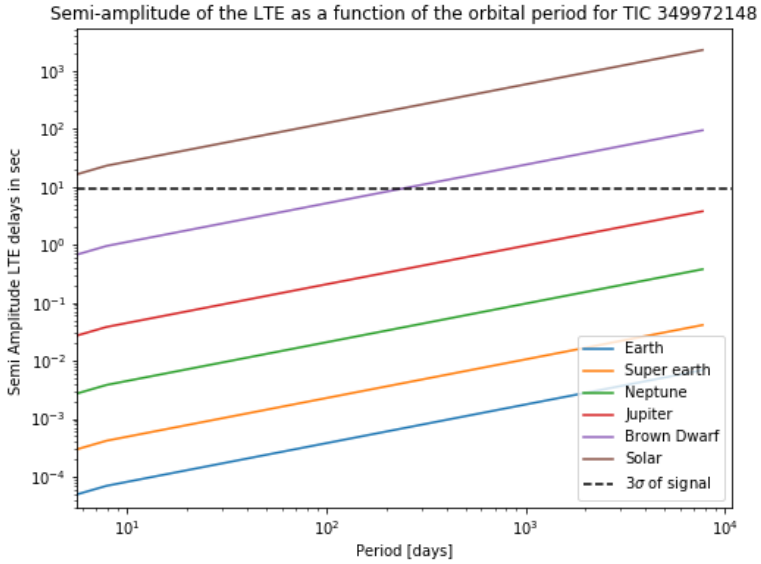


Figure 4.5: The $3\sigma$ of the RMS value of the residuals from Figure 4.3 showing the limits of detection sensitivity of orbital period of a secondary companion of Chang 414.

and an increased temporal baseline.

Subtracting the model for the stellar secondary companion, I calculated the residuals of the $O-C$ plot to see if there remains any other periodic signal that might be due to a planetary mass companion. I extracted a periodogram on the residuals (Figure 4.8) from which gave multiple peaks with low and comparable GLS Power, which might indicate that the residual signals are just noise or they are not very well time calibrated in TESS while taking the observations. In any case, I tried fitting a non-linear fit function (Equation 4.4) using the MCMC algorithm to see how well it fits. The return showed a reduced $\chi^2 = 17.66$ which shows the actual

| Parameter | Best Fit value $\pm\sigma$ |
|---|---|
| $a_0$ | 210.81 $\pm$ 0.76 |
| $a_1$ | 0.01290 $\pm$ 0.00044 |
| $a_2$ | 9.28634e-06 $\pm$ 7.39843e-07 |
| $A_0$ | 265.75 $\pm$ 0.84 sec |
| $P_{orb}$ | 803.39 $\pm$ 0.19 days |
| $\phi_0$ | -0.25734 $\pm$ 0.00066 |

Table 4.3: Parameters from the non-linear fit to the initial $O-C$ plot of Chang 451

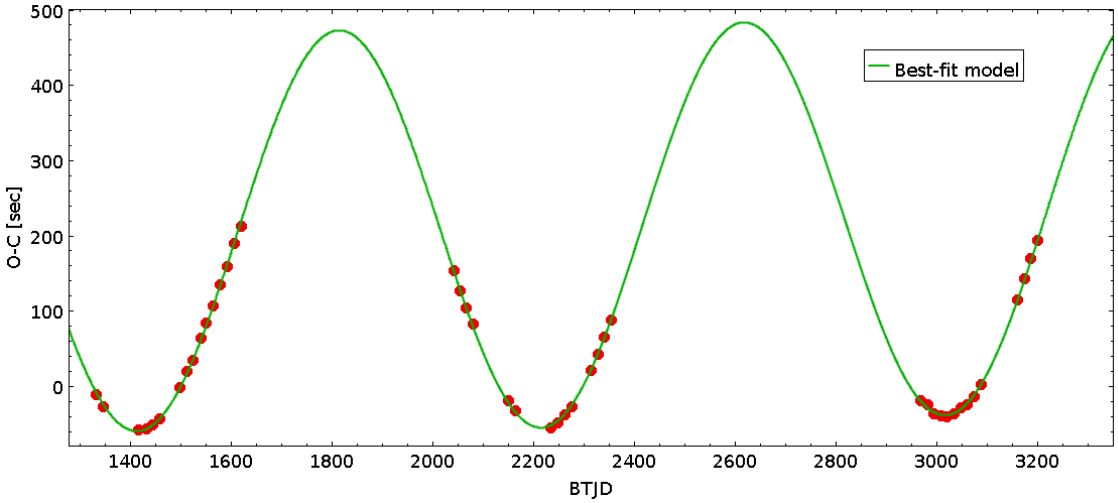


Figure 4.6: Best fit model of Equation 4.5 on the $O-C$ plot of Chang 451.

| Parameter | Obtained from Best fit values | Yang 2021 |
|---|---|---|
| Period[days] | $803.39 \pm 0.19$ | $803.5 \pm 0.6$ |
| Mass $[M_\odot]$ | $0.412 \pm 0.038$ | 0.49 |

Table 4.4: Comparison of the orbital parameters I got from MCMC analysis with the one in literature.

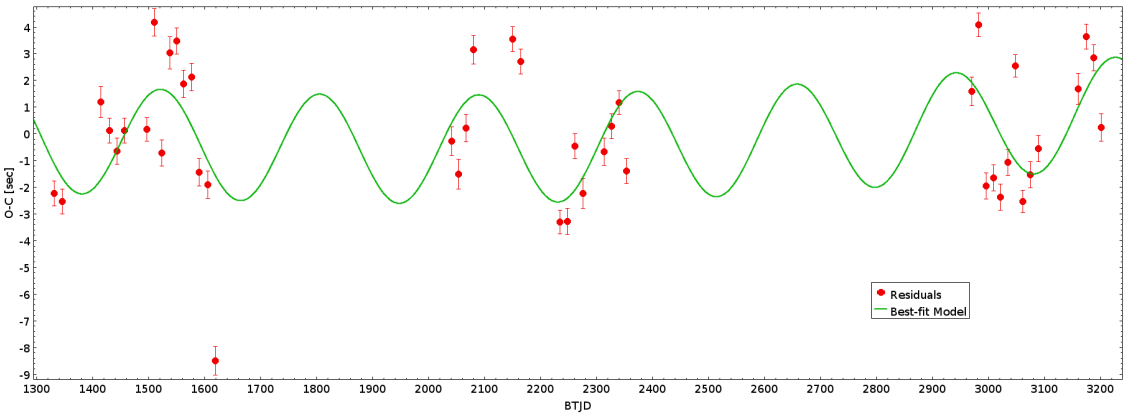


Figure 4.7: The Best-fit (polynomial + harmonic) model on the residuals of the $O-C$ plot of Chang 451.

data and the fit model do not agree with each other. Thus it can be concluded as noise. The RMS of the residual is 2.50 sec, which gives an indication of the parameter space of the perturbing companions which can be discarded. I used a $3\sigma$ RMS signal to plot on Figure 3.29 and Figure 3.30 to check for sensitivity till which we can detect companions. The RMS value being of the order of a few seconds signifies that residuals we get are pure noise, since TESS timing accuracy of order of few seconds cannot be trusted.(Discussed in Section 4.2)

From Figures 4.9 and 4.10, I concluded that I can exclude perturbers of mass Brown dwarfs(and above) of periods greater than 100 days. The TESS span of light curves for Chang 451 which I have analyzed in the thesis is of nearly 1869 days, thus the upper limit of the orbital period till which we can detect any perturbing companion is 1869 days.

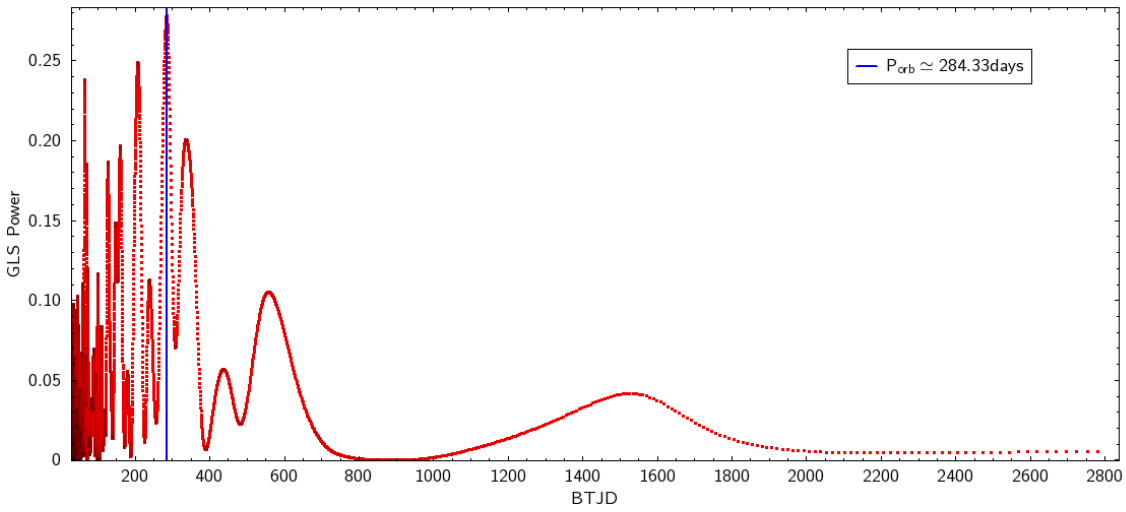


Figure 4.8: Periodogram on the residuals of Chang 451 after whitening the signal from the stellar companion.

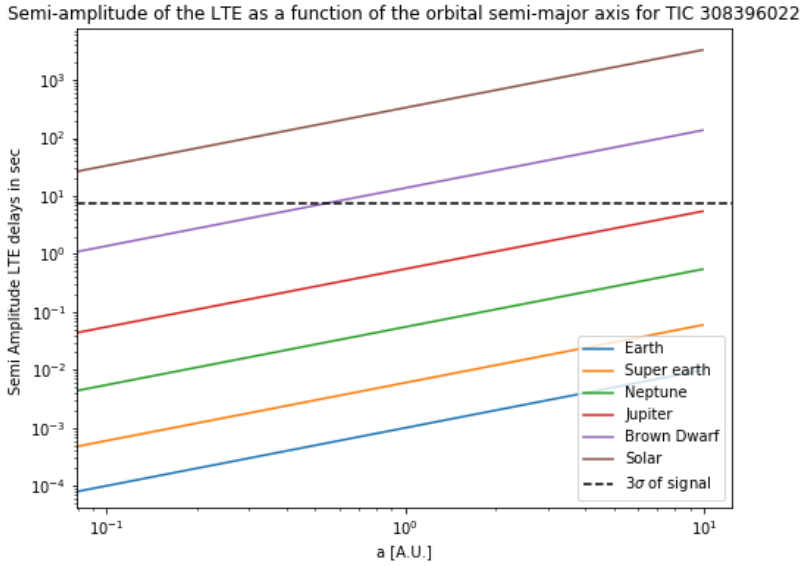


Figure 4.9: The $3\sigma$ of the RMS value of the residauls from Figure 4.7 showing the limits of detection sensitivity of orbital semi-major axis of a secondary companion of Chang 451.

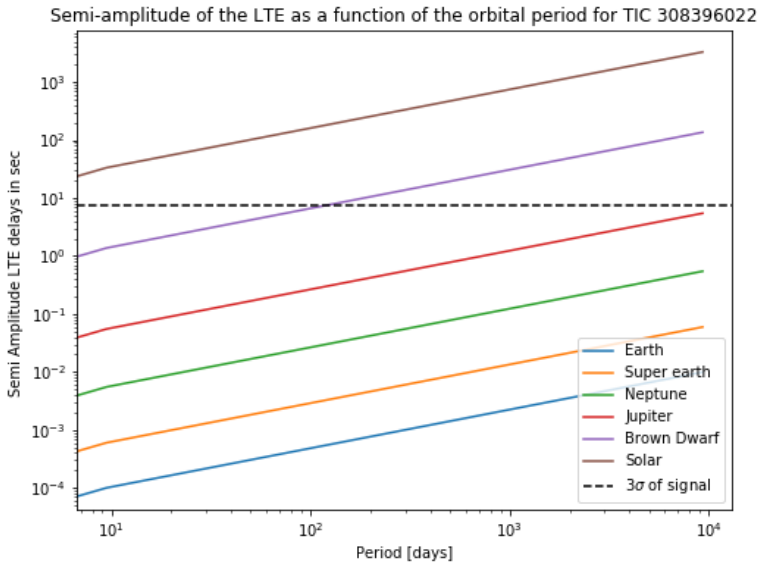


Figure 4.10: The $3\sigma$ of the RMS value of the residuals from Figure 4.7 showing the limits of detection sensitivity of orbital period of a secondary companion of Chang 451.

## 4.2 Discussion and future works

The residual signals that I got from the best fit LTTE models (Figure:4.3,4.7) have a very low RMS value of the order of a few seconds. In Figure 4.3 almost half the number of data points are consistent with 0 within the error bars. These values cannot be trusted because of the systematic errors of the absolute calibration on time stamps by TESS. This issue has been anticipated by the TESS team, and they have reported the systematic offsets of time calibration in several sectors on the TESS data release notes (DRN[1]). An independent study by Essen et al. (2020) tried to analyze the absolute time calibration of TESS. They used ground and space-based observations of primary eclipses of several binary systems in the Southern ecliptic hemisphere to verify the reliability of the TESS timestamps. They found a time offset of $5.8 \pm 2.5$sec. Thus to increase the sensitivity of the PT method, accurate calibration of TESS time stamps is necessary. During the target selection process, I encountered many targets that had not been observed by TESS for more than 10 sectors. Thus I had limitations in the choice of targets to choose from for a long baseline of observation. TESS keeps on observing targets and providing a long baseline of photometric data, which increases the number of targets that could be analysed and also increases the sensitivity of PT technique to detect smaller planetary mass companions.

The upcoming PLATO mission will have long-pointing fields, initially observing the field of view (LOPS2) continuously for two years. The extended missions have not been decided yet, but there is a possibility for PLATO to observe the same field for a longer time period. PLATO with its high-precision photometry and long baseline data will provide high-quality data for the PT technique to detect small mass planets. PLATO is also optimized to carry out asteroseismological observations, thus will provide accurate timing observations. By mission requirement, the accuracy of time stamps will be within 1 second.

My thesis was focused on a small sample because it is a pilot study analysing the properties of existing data on the PT technique. The PT technique can be applied to other variable stars such as RR Lyrae and Cepheid variables, thus applying to a bigger sample of variables can infer the population properties of the stars and their companions. I analysed stars in the LOPS2 field, but carrying out the analysis in other regions of the sky can give weightage to candidate star hosting planets. These targets could be suggested for the General Observer Program of PLATO for a longer observation and ground-based follow-up observations can be carried out. Interesting candidates can be added to the PLATO objects of interest catalog and could be used for other future missions such as ESA's M4 class mission ARIEL (The Atmospheric Remote-Sensing Infrared Exoplanet Large-survey) set to launch for 2029 (Pascale

[1] https://archive.stsci.edu/tess/tess_drn.html

et al., 2018). ARIEL will survey more than 1000 exoplanets from rocky to gas giants and the activity of its host stars through multi-band optical photometry and infrared spectroscopy. Both PLATO and ARIEL will be beneficial in providing information about variable host stars and more pre-mission analysis of variables, like my thesis work, will benefit these space missions in identifying potential candidates.

# Chapter 5

# Conclusions

I have used the Pulsation Timing(PT) Technique to detect and characterize possible secondary companions around Delta Scuti stars. My focus was on single pulsation Delta Scuti stars present in the first field of view(LOPS2) of ESA's upcoming PLATO space mission to be launched in 2026. The PT technique which is a photometric approach, is based on the fact that the presence of a secondary companion around a variable star causes movements of the host star around its barycentre, which in turn produces phase shifts of the pulsation modes of the variable stars. The technique becomes more sensitive to detect less massive planets with a long baseline of time series photometry. In this work, I have used TESS's 2-minute short cadence light curves of Delta Scuti stars which have stable and short pulsation periods (0.02 to 0.25 days). Starting with the list of known Delta Scuti stars identified by Chang et al. (2013), I matched them with the TESS CTL and filtered for stars in the first PLATO field. From there, I selected bright targets ($\text{TESS}_{mag} < 13$) that had data from more than 10 TESS sectors, resulting in a final sample of 9 suitable targets. After an initial periodogram analysis, I focused on two favorable stars for an in-depth study: TIC 349972148 (10 sectors) and TIC 308396022 (22 sectors).

Using the VARTOOLS program, I first filtered the TESS light curves of these candidates and computed their periodograms. Then I fitted a harmonic curve on each TESS orbit ($\sim 14$ days) based on the stars' fundamental pulsation period and analyzed the $O-C$ (observed minus calculated) plot to search for phase shifts of the main pulsation mode over time. I applied both a traditional least squares approach for initial estimation and a more rigorous Monte Carlo Markov Chain approach for the harmonic fit to estimate the uncertainties of the best-fit parameters.

For TIC 349971248 (Mass $= 2.15 \pm 0.10 M_{\odot}$), I detrended the $O-C$ plot for long-term trends and analyzed the residuals for any periodic variation but did not detect any perturbing companion. For TIC 308396022(Mass $= 1.50 \pm 0.13 M_{\odot}$), I observed a clear sinusoidal variation of the phase in the $O-C$ plot. By fitting a harmonic curve to the $O-C$ plot(assuming a circular and edge-on orbit), I determined the

semi-amplitude of the LTTE and the orbital period of this variation. Using these parameters, I calculated the orbital semi-major axis and the mass of the companion causing the perturbation. Thus, for TIC 308396022, I identified a secondary stellar companion with a mass of $0.41 \pm 0.03[M_{\odot}]$, an orbital period of $803.4 \pm 0.2$ days, and a projected orbital semi-major axis of $1.93 \pm 0.06$ AU. This stellar mass companion was also found by Yang et al. (2021) , but my analysis was done with more TESS sector data, hence I could characterize the companion accurately. After removing the signal of the stellar companion, I analyzed the residuals for any other periodic variation.

In both candidates, I did not detect any additional perturbing companion, but I thoroughly explored the parameter space through my analysis of the expected LTTE signal for each target. I confirmed the absence of any secondary companion in the brown-dwarf mass range (and above) with an orbital period greater than 100 days. The accuracy limitations of the absolute TESS timestamps (on the order of a few seconds) and the lack of long baseline observations for the targets presented challenges to my PT method analysis.

From the results, I concluded that the PT technique is a useful technique for the photometric evaluation of host stars. It can successfully detect secondary companions of the stellar mass regime, and with the currently available data, the sensitivity can go to the brown dwarf range. It has a bias towards massive and long-orbit companions as they produce a large LTTE signal.

# Bibliography


[1] C. Alcock, R. A. Allsman, D. R. Alves, T. S. Axelrod, A. C. Becker, D. P. Bennett, K. H. Cook, N. Dalal, A. J. Drake, K. C. Freeman, M. Geha, K. Griest, M. J. Lehner, S. L. Marshall, D. Minniti, C. A. Nelson, B. A. Peterson, P. Popowski, M. R. Pratt, P. J. Quinn, C. W. Stubbs, W. Sutherland, A. B. Tomaney, T. Vandehei, and D. Welch. The MACHO Project: Microlensing Results from 5.7 Years of Large Magellanic Cloud Observations. , 542(1):281–307, October 2000. doi: 10.1086/309512.

[2] F. Anders, A. Khalatyan, A. B. A. Queiroz, C. Chiappini, J. Ardèvol, L. Casamiquela, F. Figueras, Ó. Jiménez-Arranz, C. Jordi, M. Monguió, M. Romero-Gómez, D. Altamirano, T. Antoja, R. Assaad, T. Cantat-Gaudin, A. Castro-Ginard, H. Enke, L. Girardi, G. Guiglion, S. Khan, X. Luri, A. Miglio, I. Minchev, P. Ramos, B. X. Santiago, and M. Steinmetz. Photo-astrometric distances, extinctions, and astrophysical parameters for Gaia EDR3 stars brighter than G = 18.5. , 658:A91, February 2022. doi: 10.1051/0004-6361/202142369.

[3] William J. Borucki et al. Kepler Planet-Detection Mission: Introduction and First Results. *Science*, 327(5968):977, February 2010. doi: 10.1126/science.1185402.

[4] Dominic M. Bowman. *Amplitude Modulation of Pulsation Modes in Delta Scuti Stars*. 2017. doi: 10.1007/978-3-319-66649-5.

[5] M. Breger. $\delta$ Scuti stars (Review). In Michel Breger and Michael Montgomery, editors, *Delta Scuti and Related Stars*, volume 210 of *Astronomical Society of the Pacific Conference Series*, page 3, January 2000.

[6] D. W. Kurtz C.Aerts, J. Christensen-Dalsgaard. *Asteroseismology*. Springer Dordrecht, 2010.

[7] S.-W. Chang, P. Protopapas, D.-W. Kim, and Y.-I. Byun. Statistical properties of galactic scuti stars: Revisited. *The Astronomical Journal*, 145(5):132, mar 2013. doi: 10.1088/0004-6256/145/5/132. URL https://dx.doi.org/10.1088/0004-6256/145/5/132.

[8] D. L. Compton, T. R. Bedding, S. J. Murphy, and D. Stello. Binary star detectability in Kepler data from phase modulation of different types of oscillations. , 461(2):1943–1949, September 2016. doi: 10.1093/mnras/stw1092.

[9] Carolina von Essen, Mikkel N. Lund, Rasmus Handberg, Marina S. Sosa, Julie Thiim Gadeberg, Hans Kjeldsen, Roland K. Vanderspek, Dina S. Mortensen, M. Mallonn, L. Mammana, Edward H. Morgan, Jesus Noel S. Villaseñor, Michael M. Fausnaugh, and George R. Ricker. Tess data for asteroseismology: Timing verification*. *The Astronomical Journal*, 160(1):34, June 2020. ISSN 1538-3881. doi: 10.3847/1538-3881/ab93dd. URL http://dx.doi.org/10.3847/1538-3881/ab93dd.

[10] Jonathan P. Gardner, John C. Mather, Mark Clampin, Rene Doyon, Matthew A. Greenhouse, Heidi B. Hammel, John B. Hutchings, Peter Jakobsen, Simon J. Lilly, Knox S. Long, Jonathan I. Lunine, Mark J. McCaughrean, Matt Mountain, John Nella, George H. Rieke, Marcia J. Rieke, Hans-Walter Rix, Eric P. Smith, George Sonneborn, Massimo Stiavelli, H. S. Stockman, Rogier A. Windhorst, and Gillian S. Wright. The James Webb Space Telescope. , 123(4):485–606, April 2006. doi: 10.1007/s11214-006-8315-7.

[11] Gerald Handler. Delta Scuti Variables. In Joyce Ann Guzik and Paul A. Bradley, editors, *Stellar Pulsation: Challenges for Theory and Observation*, volume 1170 of *American Institute of Physics Conference Series*, pages 403–409. AIP, September 2009. doi: 10.1063/1.3246528.

[12] Gerald Handler. *Asteroseismology*, pages 207–241. Springer Netherlands, Dordrecht, 2013. ISBN 978-94-007-5615-1. doi: 10.1007/978-94-007-5615-1_4. URL https://doi.org/10.1007/978-94-007-5615-1_4.

[13] J. J. Hermes. *Timing by Stellar Pulsations as an Exoplanet Discovery Method*, page 787–796. Springer International Publishing, 2018. doi: 10.1007/978-3-319-55333-7_6. URL http://dx.doi.org/10.1007/978-3-319-55333-7_6.

[14] John B. Irwin. The Determination of a Light-Time Orbit. , 116:211, July 1952. doi: 10.1086/145604.

[15] H. Jin, S. L. Kim, C. U. Lee, D. J. Lee, and K. S. Kim. Reclassification of ROTSE-I $\delta$ Scuti Stars with Multiband Photometry and Fourier Decomposition. , 128(4):1847–1856, October 2004. doi: 10.1086/423908.

[16] D. W. Kim, P. Protopapas, C. Alcock, Y. I. Byun, J. Kyeong, B. C. Lee, N. J. Wright, T. Axelrod, F. B. Bianco, W. P. Chen, N. K. Coehlo, K. H. Cook,

R. Dave, S. K. King, T. Lee, M. J. Lehner, H. C. Lin, S. L. Marshall, R. Porrata, J. A. Rice, M. E. Schwamb, J. H. Wang, S. Y. Wang, C. Y. Wen, and Z. W. Zhang. The Taiwan-American Occultation Survey Project Stellar Variability. I. Detection of Low-Amplitude $\delta$ Scuti Stars. , 139(2):757–764, February 2010. doi: 10.1088/0004-6256/139/2/757.

[17] M. Kiraga. ASAS Photometry of ROSAT Sources. I. Periodic Variable Stars Coincident with Bright Sources from the ROSAT All Sky Survey. , 62(1):67–95, March 2012. doi: 10.48550/arXiv.1204.3825.

[18] D. H. McNamara. Period-Luminosity Relations of SX Phoenicis Stars. , 109: 1751, April 1995. doi: 10.1086/117405.

[19] M. Montalto, G. Piotto, P. M. Marrese, V. Nascimbeni, L. Prisinzano, V. Granata, S. Marinoni, S. Desidera, S. Ortolani, C. Aerts, E. Alei, G. Altavilla, S. Benatti, A. Börner, J. Cabrera, R. Claudi, M. Deleuil, M. Fabrizio, L. Gizon, M. J. Goupil, A. M. Heras, D. Magrin, L. Malavolta, J. M. Mas-Hesse, I. Pagano, C. Paproth, M. Pertenais, D. Pollacco, R. Ragazzoni, G. Ramsay, H. Rauer, and S. Udry. The all-sky PLATO input catalogue. , 653:A98, September 2021. doi: 10.1051/0004-6361/202140717.

[20] Philip S. Muirhead, Courtney D. Dressing, Andrew W. Mann, Bárbara Rojas-Ayala, Sébastien Lépine, Martin Paegert, Nathan De Lee, and Ryan Oelkers. A catalog of cool dwarf targets for the transiting exoplanet survey satellite. *The Astronomical Journal*, 155(4):180, apr 2018. doi: 10.3847/1538-3881/aab710. URL https://dx.doi.org/10.3847/1538-3881/aab710.

[21] S. J. Murphy, A. Pigulski, D. W. Kurtz, J. C. Suárez, G. Handler, L. A. Balona, B. Smalley, K. Uytterhoeven, R. Szabó, A. O. Thygesen, V. Elkin, M. Breger, A. Grigahcène, J. A. Guzik, J. M. Nemec, and J. Southworth. Asteroseismology of KIC 11754974: a high-amplitude SX Phe pulsator in a 343-d binary system. , 432(3):2284–2297, July 2013. doi: 10.1093/mnras/stt587.

[22] Simon J. Murphy, Timothy R. Bedding, and Hiromoto Shibahashi. A Planet in an 840 Day Orbit around a Kepler Main-sequence A Star Found from Phase Modulation of Its Pulsations. , 827(1):L17, August 2016. doi: 10.3847/2041-8205/827/1/L17.

[23] V. Nascimbeni, G. Piotto, A. Börner, M. Montalto, P. M. Marrese, J. Cabrera, S. Marinoni, C. Aerts, G. Altavilla, S. Benatti, R. Claudi, M. Deleuil, S. Desidera, M. Fabrizio, L. Gizon, M. J. Goupil, V. Granata, A. M. Heras, D. Magrin, L. Malavolta, J. M. Mas-Hesse, S. Ortolani, I. Pagano, D. Pollacco, L. Prisinzano, R. Ragazzoni, G. Ramsay, H. Rauer, and S. Udry. The PLATO

field selection process. I. Identification and content of the long-pointing fields. , 658:A31, February 2022. doi: 10.1051/0004-6361/202142256.

[24] Martin Paegert, Keivan G. Stassun, Karen A. Collins, Joshua Pepper, Guillermo Torres, Jon Jenkins, Joseph D. Twicken, and David W. Latham. TESS Input Catalog versions 8.1 and 8.2: Phantoms in the 8.0 Catalog and How to Handle Them. *arXiv e-prints*, art. arXiv:2108.04778, August 2021. doi: 10.48550/arXiv.2108.04778.

[25] Enzo Pascale et al. The ARIEL space mission. In Makenzie Lystrup, Howard A. MacEwen, Giovanni G. Fazio, Natalie Batalha, Nicholas Siegler, and Edward C. Tong, editors, *Space Telescopes and Instrumentation 2018: Optical, Infrared, and Millimeter Wave*, volume 10698 of *Society of Photo-Optical Instrumentation Engineers (SPIE) Conference Series*, page 106980H, July 2018. doi: 10.1117/12.2311838.

[26] M. A. C. Perryman, L. Lindegren, J. Kovalevsky, E. Hoeg, U. Bastian, P. L. Bernacca, M. Crézé, F. Donati, M. Grenon, M. Grewing, F. van Leeuwen, H. van der Marel, F. Mignard, C. A. Murray, R. S. Le Poole, H. Schrijver, C. Turon, F. Arenou, M. Froeschlé, and C. S. Petersen. The HIPPARCOS Catalogue. , 323:L49–L52, July 1997.

[27] G. Pojmanski, Gracjan Maciejewski, Bogumił Pilecki, and D. Szczygiel. Asas variable stars in southern hemisphere (pojmanski+, 2002-2005). *VizieR Online Data Catalog*, 07 2006.

[28] Andrej Prša, Angela Kochoska, Kyle E. Conroy, Nora Eisner, Daniel R. Hey, et al. TESS Eclipsing Binary Stars. I. Short-cadence Observations of 4584 Eclipsing Binaries in Sectors 1-26. , 258(1):16, January 2022. doi: 10.3847/1538-4365/ac324a.

[29] H. Rauer et al. The PLATO 2.0 mission. *Experimental Astronomy*, 38(1-2): 249–330, November 2014. doi: 10.1007/s10686-014-9383-4.

[30] Heike Rauer et al. The PLATO Mission. *arXiv e-prints*, art. arXiv:2406.05447, June 2024. doi: 10.48550/arXiv.2406.05447.

[31] George R. Ricker et al. Transiting Exoplanet Survey Satellite (TESS). *Journal of Astronomical Telescopes, Instruments, and Systems*, 1:014003, January 2015. doi: 10.1117/1.JATIS.1.1.014003.

[32] E. Rodríguez and M. J. López-González. SX Phe stars in globular clusters. , 359:597–600, July 2000.

[33] N. N. Samus, E. V. Kazarovets, O. V. Durlevich, N. N. Kireeva, and E. N. Pastukhova. VizieR Online Data Catalog: General Catalogue of Variable Stars (Samus+, 2007-2017). VizieR On-line Data Catalog: B/gcvs. Originally published in: 2017ARep...61...80S; 2017AZh....94...87S, January 2009.

[34] R. Silvotti, S. Schuh, R. Janulis, J. E. Solheim, S. Bernabei, R. Østensen, T. D. Oswalt, I. Bruni, R. Gualandi, A. Bonanno, G. Vauclair, M. Reed, C. W. Chen, E. Leibowitz, M. Paparo, A. Baran, S. Charpinet, N. Dolez, S. Kawaler, D. Kurtz, P. Moskalik, R. Riddle, and S. Zola. A giant planet orbiting the 'extreme horizontal branch' star V391 Pegasi. , 449(7159):189–191, September 2007. doi: 10.1038/nature06143.

[35] Joshua S. Speagle. A conceptual introduction to markov chain monte carlo methods, 2020.

[36] Keivan G. Stassun, Ryan J. Oelkers, Martin Paegert, Guillermo Torres, Joshua Pepper, Nathan De Lee, Kevin Collins, David W. Latham, et al. The Revised TESS Input Catalog and Candidate Target List. , 158(4):138, October 2019. doi: 10.3847/1538-3881/ab3467.

[37] Daniel J. Stevens and B. Scott Gaudi. A posteriori transit probabilities. *Publications of the Astronomical Society of the Pacific*, 125(930):933–950, August 2013. ISSN 1538-3873. doi: 10.1086/672572. URL http://dx.doi.org/10.1086/672572.

[38] A. Udalski, M. Kubiak, and M. Szymanski. Optical Gravitational Lensing Experiment. OGLE-2 – the Second Phase of the OGLE Project. , 47:319–344, July 1997. doi: 10.48550/arXiv.astro-ph/9710091.

[39] V. Vaulato, V. Nascimbeni, and G. Piotto. TESS search for substellar companions through pulsation timing of $\delta$ Scuti stars. I. Discovery of companions around Chang 134 and V393 Car. , 668:A110, December 2022. doi: 10.1051/0004-6361/202244592.

[40] Tao-Zhi Yang, Zhao-Yu Zuo, Gang Li, Timothy R. Bedding, Simon J. Murphy, and Meridith Joyce. TIC 308396022: $\delta$ Scuti-$\gamma$ Doradus hybrid with large-amplitude radial fundamental mode and regular g-mode period spacing. , 655: A63, November 2021. doi: 10.1051/0004-6361/202142198.

[41] Zechmeister, M. and Kürster, M. The generalised lomb-scargle periodogram - a new formalism for the floating-mean and keplerian periodograms. *AA*, 496(2): 577–584, 2009. doi: 10.1051/0004-6361:200811296. URL https://doi.org/10.1051/0004-6361:200811296.